Assessment of the INRIM trace water generator and analysis of the uncertainty components down to -100 °C frost-point temperature

Original

Assessment of the INRIM trace water generator and analysis of the uncertainty components down to -100 °C frost-point temperature / Cuccaro, Rugiada; Beltramino, Giulio; Rosso, Lucia; Nobakht, Rezvaneh; Fernicola, V. - In: METROLOGIA. - ISSN 0026-1394. - ELETTRONICO. - 61:4(2024). [10.1088/1681-7575/ad53cc]

Publisher:
IOP Publishing Ltd

Published
DOI:10.1088/1681-7575/ad53cc

Metrologia

ACCEPTED MANUSCRIPT • OPEN ACCESS

Assessment of the INRIM trace water generator and analysis of the uncertainty components down to -100 °C frost-point temperature

To cite this article before publication: Rugiada Cuccaro *et al* 2024 *Metrologia* in press https://doi.org/10.1088/1681-7575/ad53cc

Manuscript version: Accepted Manuscript

Accepted Manuscript is “the version of the article accepted for publication including all changes made as a result of the peer review process, and which may also include the addition to the article by IOP Publishing of a header, an article ID, a cover sheet and/or an ‘Accepted Manuscript’ watermark, but excluding any other editing, typesetting or other changes made by IOP Publishing and/or its licensors”

This Accepted Manuscript is **© 2024 The Author(s). Published on behalf of BIPM by IOP Publishing Ltd**.

As the Version of Record of this article is going to be / has been published on a gold open access basis under a CC BY 4.0 licence, this Accepted Manuscript is available for reuse under a CC BY 4.0 licence immediately.

Everyone is permitted to use all or part of the original content in this article, provided that they adhere to all the terms of the licence https://creativecommons.org/licences/by/4.0

Although reasonable endeavours have been taken to obtain all necessary permissions from third parties to include their copyrighted content within this article, their full citation and copyright line may not be present in this Accepted Manuscript version. Before using any content from this article, please refer to the Version of Record on IOPscience once published for full citation and copyright details, as permissions may be required. All third party content is fully copyright protected and is not published on a gold open access basis under a CC BY licence, unless that is specifically stated in the figure caption in the Version of Record.

View the article online for updates and enhancements.

This content was downloaded from IP address 130.192.232.228 on 11/06/2024 at 16:48

Assessment of the INRIM trace water generator and analysis of the uncertainty components down to -100 °C frost-point temperature

Rugiada Cuccaro[1], Giulio Beltramino[1], Lucia Rosso[1], Rezvaneh Nobakht[1,2] and Vito Fernicola[1]

[1] INRIM – Istituto Nazionale di Ricerca Metrologica, Torino, 10135, Italy
[2] Politecnico di Torino, Torino, 10129, Italy

E-mail: r.cuccaro@inrim.it

Received xxxxxx
Accepted for publication xxxxxx
Published xxxxxx

Abstract

A low frost-point generator (INRIM 03) able to operate at sub-atmospheric pressure has been recently designed, constructed, and assessed at the Istituto Nazionale di Ricerca Metrologica (INRiM) with the aim of providing the metrological traceability both to instruments developed for the measurement of humidity in atmosphere and to sensors and analysers used in industry for controlling and measuring the amount of water vapour in manufacturing processes.

The humidity generator operates in a single temperature single pressure mode, letting the carrier gas (nitrogen) achieve saturation in a single passage through an isothermal saturator. Its working range encompasses a frost-point temperature range from -100 °C to -20 °C, in a pressure range between 200 hPa and 1100 hPa, corresponding to an amount of water fraction range from $13 \cdot 10^{-9}$ mol·mol^{-1} to $6.2 \cdot 10^{-3}$ mol·mol^{-1}.

In a previous work its performance was assessed in the frost-point temperature range from -75 °C to -20 °C [2]. In this work, a comprehensive set of tests for its characterisation and performance evaluation between -75 °C and -100 °C is presented. A detailed uncertainty analysis in the above temperature range is reported, taking into account all the sources of uncertainty that affect the humid gas generation. An expanded uncertainty (k=2) of 0.07 °C was found for frost-point temperature measurements between -75 °C and -95 °C, while an expanded uncertainty of 0.26 °C resulted at a frost-point temperature of -100 °C. The relative expanded uncertainty (k=2) associated with water vapour amount fraction measurements was estimated equal to or better than 1.2 % between $35 \cdot 10^{-9}$ mol·mol^{-1} and $6.1 \cdot 10^{-3}$ mol·mol^{-1}, increasing up to 6.5 % at $13 \cdot 10^{-9}$ mol·mol^{-1}.

Keywords: hygrometry, humidity standard, frost point, trace water measurement

---

1. Introduction

In the present context in which climate change and environmental degradation have been recognised as a real threat to Europe and the world, the European Commission delivered the European Green Deal, an ambitious package of policy initiatives, which aims to set the EU on the path to a green transition, with a climate neutrality goal by 2050 [1]. Water vapour is a remarkable gaseous source of infrared opacity in the atmosphere, representing one of the main greenhouse gases. For this reason, it has been included among the so-called essential climate variables (ECVs), identified by the global climate observing system to be monitored as critical drivers of Earth's climate changes. Its accurate measurement is challenging as the water vapour amount fraction decreases from some percent to a few parts per million moving from the ground level to the stratosphere. Different research groups have focused their efforts in the realisation of humidity standards able to generate a humid gas with a water vapour amount fraction less than $1\cdot10^{-6}$ mol/mol (1 ppm), in order to provide the metrological traceability to all the instruments developed for the measurement of humidity in the atmosphere [2-6].

A higher accuracy in controlling and measuring the water vapour also below $1\cdot10^{-6}$ mol/mol is of interest for industry, due to the significant effects that water vapour has on product quality, production efficiency and costs, and consequently on waste generation. In ultra-high purity (UHP) process gases, trace water is the single largest matrix contaminant and affects the process yield in UHP gas applications such as the semiconductor manufacturing, where a trace water contamination of a few parts per billion can result in failure in microelectronic units. Enhanced process efficiency in fabrication processes also allows reduced use of toxic chemicals, reduced waste of raw materials, reduced need for re-work, recovery, and re-processing, contributing to the reduction of energy consumption and carbon emissions.

As mentioned in Cuccaro *et al.* [2], over the last decade trace humidity generators have been realised in the several metrological institutes around the world. At the National Metrology Institute of Japan (NMIJ) a diffusion tube humidity generator (DTG) based on the molecular diffusion was developed as a possible alternative to the frost-point generator [3-6]. By an accurate control of flow, temperature and pressure, that generator produces humid nitrogen in the trace water range with a relative standard uncertainty of the order of 0.2 %. At the Korea Research Institute of Standards and Science (KRISS) a frost-point generator (LFPG 2) was developed [7]. Previously, the KRISS had developed a low frost-point generator named LFPG 1 able to produce a humid gas with a frost-point temperature down to -105 °C. It was based on a saturator cooled by means of a refrigeration and thermoelectric systems and operated in a two-temperature, two-pressure (2T-2P) mode [8-10]. The new LFPG 2 also operates in the 2T-2P mode and is based on a saturator hosted in a thermostatic bath. The expanded measurement uncertainty (k=2) for the humidity generation range between 7 nmol·mol^{-1} to 1000 nmol·mol^{-1} varies between 0.33 nmol·mol^{-1} and 9.9 nmol·mol^{-1}, respectively, equivalent to 5 % and 1 % in relative expanded uncertainty. Compared with LFPG 1, the measurement uncertainty improved by about a factor of two.

In the recent past, the Swiss Designated Institute for humidity, MBW Calibration AG, developed a new humidity standard generator to be used as the primary realisation of the frost point temperature between -90 °C and -10 °C [11]. The generator worked in a single pressure mode for saturation temperatures between -80 °C and -10 °C and in two-pressure mode for saturation temperatures down to -90 °C. When used in single pressure mode the frost point temperature corresponds to the temperature at which the carrier gas is saturated (after applying corrections for pressure drops towards the point of use), while in the two-pressure mode the carrier gas is saturated at a pressure higher than the ambient and subsequently expanded passing through an expansion metering valve. In the frost-point temperature range between -90 °C and -80 °C, the stated expanded uncertainty (coverage factor k =2) ranges between 0.40 °C and 0.20 °C.

Another notable example of low frost-point primary humidity generator was developed at the UK National Physical Laboratory (NPL). The humidity generator is suitable for operation in two-temperature or two-pressure mode over the frost-point temperature range from -95 °C to -10 °C with saturator pressures up to 3.5 MPa. The saturator has a modular design consisting of coiled pipes attached to a central manifold which provides structural rigidity, restraining the coils when used in two-pressure mode. Horizontal coils are connected by inclined tubes and each coil can be removed, so that the operation of the saturator and its efficiency can be examined in detail as well as, in order to simplify periodic pipe maintenance operations [12].

Recently, at the Istituto Nazionale di Ricerca Metrologica (INRIM) a low frost-point primary generator able to operate from sub-atmospheric pressure has been designed and constructed. The generator, named INRIM 03, covers the frost point temperature range between -100 °C and -20 °C, and operates in the pressure range between 1100 hPa and 200 hPa. A description of the generator and its performance were assessed in the frost-point temperature range from -75 °C to -20 °C with the aim of providing SI traceable calibration to radiosondes and reported by Cuccaro *et al.* [2].

In this work, after a brief description of the experimental apparatus, the results of a comprehensive set of tests carried out to validate the individual uncertainty components are presented. Detailed uncertainty evaluations of both the frost-point temperature and the water vapour amount fraction are given in the whole working pressure range and in the frost-point temperature range between -75 °C and -100 °C.

2. Theory of operation

The INRIM 03 generator is based on the single temperature, single pressure principle (1T-1P), where the measured frost point temperature T_{fp} only depends on the saturation temperature T_{sat} (except for a small pressure drops toward the point of use). Assuming that the water saturator pathway is long enough to ensure the full saturation of the input gas in a single passage, the carrier gas which flows through the saturator is able to reach its thermodynamic equilibrium over a plane surface of isothermal ice maintained at a temperature T_{sat} and a pressure p. Therefore, the water vapour amount fraction, x_{w}, at the generator gas outlet is determined by the equation:

$$x_{\mathrm{w}} = \frac{f(T_{\mathrm{sat}}, p) \cdot e_{\mathrm{w}}(T_{\mathrm{sat}})}{p} \tag{1}$$

where $e_{\mathrm{w}}(T_{\mathrm{sat}})$ is the saturation vapour pressure over ice at the temperature T_{sat}, p is the total system pressure and $f(T_{\mathrm{sat}}, p)$ is the water vapour enhancement factor, which takes into account the non-ideal behaviour of the gas mixture. Unlike the previous work [2], where the empirical formulation of Sonntag [13] was used for the determination of the saturation vapour pressure over ice, in this work the quantity $e_{\mathrm{w}}(T_{\mathrm{sat}})$ and its relative standard uncertainty $u_{\mathrm{r}}(e_{\mathrm{w}})$, have been estimated by using the formulation given by the 2011 IAPWS release for the sublimation pressure of ice Ih [14], also reported in the article by Wagner *et al.* [15]. The authors have chosen to use the most recent formulations for $e_{\mathrm{w}}(T_{\mathrm{sat}})$ and $u_{\mathrm{r}}(e_{\mathrm{w}})$, although the numerical difference between the values of $e_{\mathrm{w}}(T_{\mathrm{sat}})$ given by Sonntag's and Wagner's formulation is often negligible.

The enhancement factor $f(T_{\mathrm{sat}}, p)$ was estimated by means of the approximation function given by Bögel [16] for moist air, while the estimation of its relative uncertainty $u_{\mathrm{r}}(f)$ is based on the work of Lovell-Smith [17].

Considering that x_{w} is determined using Eq. (1), its combined standard uncertainty, $u(x_{\mathrm{w}})$, is given by:

$$u(x_{\mathrm{w}}) = \sqrt{\left[x_{\mathrm{w}}\left(\frac{1}{f}\frac{\partial f}{\partial T_{\mathrm{sat}}} + \frac{1}{e_{\mathrm{w}}}\frac{\partial e_{\mathrm{w}}}{\partial T_{\mathrm{sat}}}\right)\right]^2 \cdot u_{\mathrm{c}}^2(T_{\mathrm{sat}}) + \left[x_{\mathrm{w}}\left(\frac{1}{f}\frac{\partial f}{\partial p} - \frac{1}{p}\right)\right]^2 \cdot u_{\mathrm{c}}^2(p) + \left(\frac{e_{\mathrm{w}}}{p}\right)^2 \cdot u^2(f) + \left(\frac{f}{p}\right)^2 \cdot u^2(e_{\mathrm{w}})}\ , \tag{2}$$

where $u_{\mathrm{c}}(T_{\mathrm{sat}})$ and $u_{\mathrm{c}}(p)$ are the combined measurement uncertainties of the saturation temperature and the pressure, respectively; $u(e_{\mathrm{w}})$ and $u(f)$ are the standard uncertainties of $e_{\mathrm{w}}(T_{\mathrm{sat}})$ and $f(T_{\mathrm{sat}}, p)$, respectively; while the terms $x_{\mathrm{w}}\left(\frac{1}{f}\frac{\partial f}{\partial T_{\mathrm{sat}}} + \frac{1}{e_{\mathrm{w}}}\frac{\partial e_{\mathrm{w}}}{\partial T_{\mathrm{sat}}}\right)$, $x_{\mathrm{w}}\left(\frac{1}{f}\frac{\partial f}{\partial p} - \frac{1}{p}\right)$, $\frac{e_{\mathrm{w}}}{p}$ and $\frac{f}{p}$ are the relevant sensitivity coefficients. A detailed uncertainty analysis for T_{sat} and p is reported in section 5.

3. Experimental set up

Figure 1a presents a picture of the INRIM 03 generator hosted in a thermostatic bath, while figures 1b and 1c show a rendering of the gas lines and of the heat exchanger/saturator, which represent the core of the experimental setup. A detailed schematic of the whole system is available in [2].

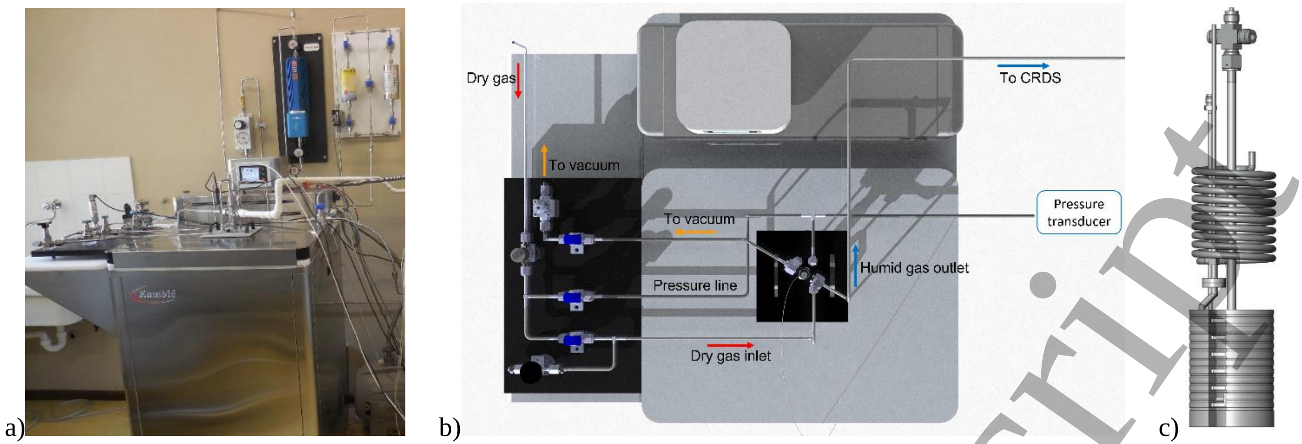

Figure 1: a) Photograph of the INRIM 03 humidity generator; b) Schematic of the generator gas lines (top view); c) Design of the heat exchanger and the ice saturator.

The saturator and the heat exchanger are immersed in a precision liquid bath: anhydrous ethanol was used as heat transfer fluid to enable operation at any temperature between -100 °C and -20 °C.

The gas saturation temperature T_{sat} is measured using a standard platinum resistance thermometer (SPRT) which is placed inside the saturator outlet pipe and results in thermal equilibrium with the saturated gas stream. In addition, the saturator bath temperature T_{bath} is also measured by means of a second platinum resistance thermometer (PRT) immersed into the ethanol bath. Both temperatures are read through a precision thermometer bridge. A PID-based electronic back-pressure regulator controls the pressure at any value in the range between 200 hPa and 1100 hPa. The experimental setup includes molecular-sieves filters at the generator gas inlet which reduces the frost-point temperature of the incoming dry gas well below -100 °C, so letting the humidity saturator always work in the evaporation mode.

The stream of dry gas, here nitrogen, flows through a 3-m helicoidal heat exchanger and then through a 3-m long isothermal saturator, with a 14 mm × 9 mm cross section whose passageways are filled at about 40 % with ice, leaving a 14 mm × 5.5 mm passageway for the flowing gas. At the exit of the saturator, the fully-saturated carrier gas can be delivered to the units under calibration - either a cavity ring-down spectroscopy (CRDS) moisture analyser or a chilled-mirror hygrometer (CMH)- via electro-polished stainless steel (EP-SS) heated tubing. For a more detailed description of the experimental apparatus refer to Cuccaro *et al* [2].

The performance of the humidity generator was assessed by means of a Tiger Optics HALO H2O RP CRDS used as a differential instrument, i.e. to detect any change in the reference value by varying the generator operating conditions. The CRDS can operate over a pressure range from 150 hPa to 2500 hPa with a specified measuring interval ranging from few parts in 10^9 (ppb) to 10 parts in 10^6 (10 ppm). This enabled the characterisation of the INRIM 03 in the whole working pressure range, although with some limitation in the lowest sub-range because of the CRDS detection limit as discussed in section 5.1.

4. Performance tests and validation of the uncertainty components between -100 °C and -75 °C

In order to evaluate the INRIM 03 performance and determine the uncertainty budget associated with the measurement of the water vapour amount fraction x_{w} and the frost-point temperature T_{fp} , the humidity generator has been subjected to several tests over its pressure and temperature operating ranges. Since the validation of the humidity generator in the frost-point temperature range between -20 °C and -75 °C at 1000 hPa had been already reported in a previous work [2], the tests were focused on the frost-point temperature range between -75 °C and -100 °C and the pressure range from 200 hPa to 1100 hPa, which corresponds to an amount of water fraction between $6.1{\cdot}10^{-6}$ mol·mol^{-1} and $13{\cdot}10^{-9}$ mol·mol^{-1}.

The experimental tests carried out and the results obtained are discussed below. They included the evaluation of the measurement repeatability and stability of the saturation temperature T_{sat}, the saturation pressure p and the flow rate ϕ, as well as the saturator efficiency and the water vapour adsorption/desorption effects on the generated humid gas.

4.1 Temperature, pressure and flow rate repeatability and stability

The water vapour amount fraction x_{w} of the humid gas depends on the saturation temperature and pressure. Gas flow rate fluctuations at the inlet of the generator may cause instability of the pressure control and, as per Eq. (1), in the generated x_{w}. On the other hands, while the frost-point temperature at the outlet is affected by the flow-dependent pressure drop in the tubing, the measured x_{w} is not, making the CRDS analyser relatively flow insensitive in contrast to e.g. chilled mirror hygrometers.

Pressure fluctuations have been investigated as a function of the gas flow rate in the range from 1 l·min^{-1} to 6 l·min^{-1} at the generation pressure and for saturation temperatures between -75 °C and -100 °C. The peak-to-peak pressure amplitude was below 100 Pa in all investigated conditions, leading to a worst-case pressure standard deviation of 20 Pa at 1100 hPa (0.02 %) and 10 Pa at 200 hPa (0.05 %). Figure 2 shows the pressure stability as a function of time at both ends of the investigated ranges, more precisely Figures 2a and 2b refer to a saturation temperature of about -100 °C at a pressure of 1100 hPa and 200 hPa, respectively; while Figures 2c and 2d refer to a saturation temperature of about -75 °C at a pressure of 1100 hPa and 200 hPa, respectively.

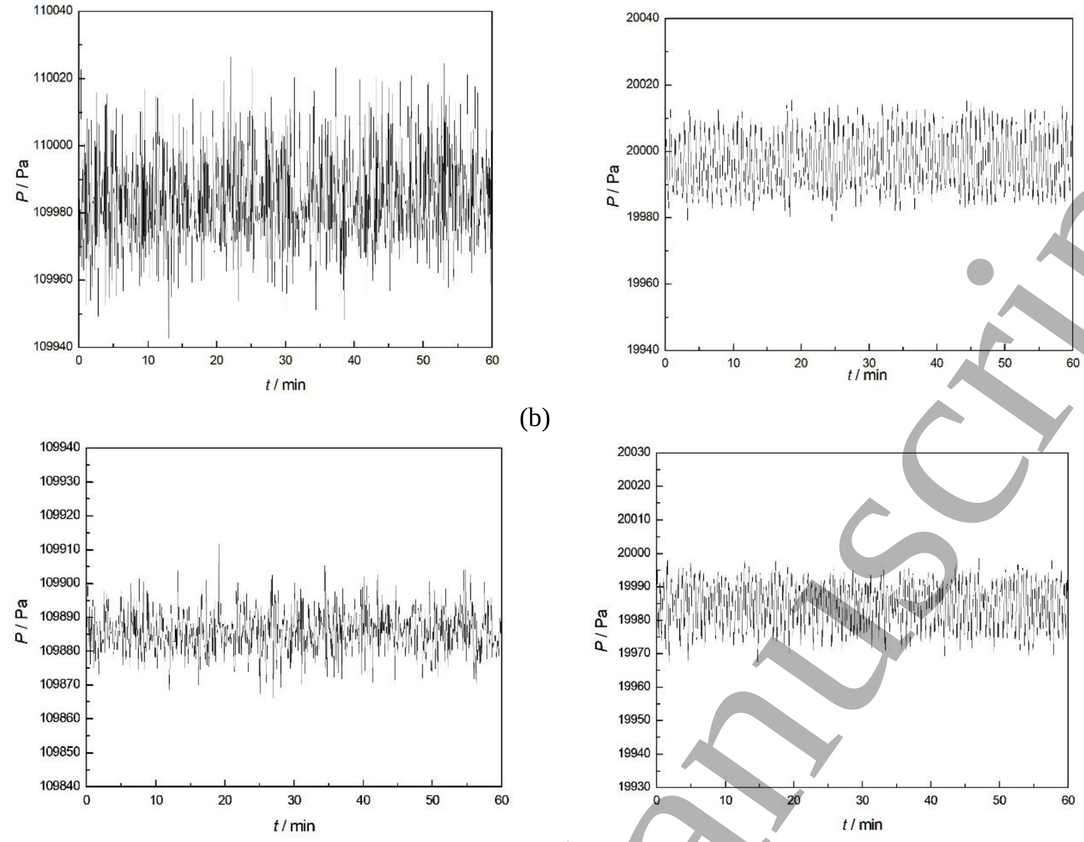

(a) (b)

(c) (d)

Figure 2: Pressure stability under the following nominal conditions: (a) ϕ = 4 l·min^{-1}, p = 1100 hPa and T_{sat} = -99.3 °C. Peak-to-peak amplitude = 0.92 hPa, mean value = 1099.85 hPa, standard deviation = 17 Pa; (b) ϕ = 1.5 l·min^{-1}, p = 200 hPa and T_{sat} = -99.3 °C. Peak-to-peak amplitude = 0.39 hPa, mean value =199.97 hPa, standard deviation = 8 Pa; (c) ϕ = 5 l·min^{-1}, p = 1100 hPa and T_{sat} = -75 °C. Peak-to-peak amplitude = 0.64 hPa, mean value = 1098.86 hPa, standard deviation = 7 Pa; (d) ϕ = 1.5 l·min^{-1}, p = 200 hPa and T_{sat} = -75 °C. Peak-to-peak amplitude = 0.35 hPa, mean value = 199.85 hPa, standard deviation = 7 Pa. All flow rates are at pressure.

The stability of the gas flow rate at the generation pressure has also been investigated independently, although the pressure stability as reported above already included the flow rate stability contribution. Figure 3 shows the variation of the flow rate at 1 l·min^{-1} at 200 hPa and at 6 l·min^{-1} at 1100 hPa, corresponding to the minimum and maximum values at which the humidity generator can operate. The highest peak-to-peak variation has been observed at the flow rate of 6 l·min^{-1}at 1100 hPa, where it reached an amplitude of about 34 ml·min^{-1} corresponding to a standard deviation of 4.6 ml·min^{-1} or 0.08 %.

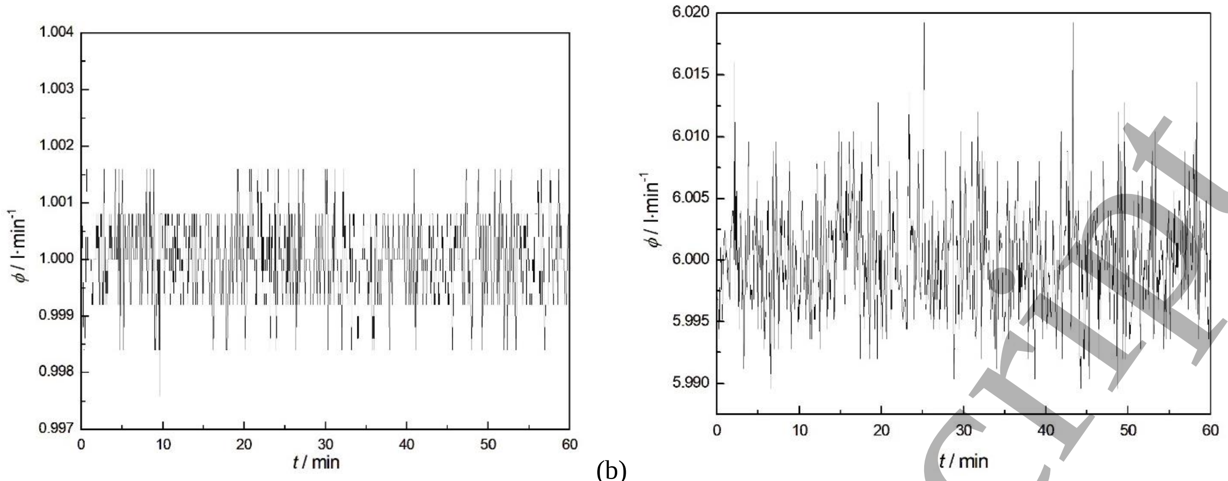

Figure 3: Flow rate stability under the following nominal conditions: (a) ϕ = 1.00 l·min^{-1}, p = 200 hPa and T_{sat} = -99 °C. Peak-to-peak amplitude = 5.6 ml·min^{-1}, mean value = 1.000 l·min^{-1}, standard deviation = 0.8 ml·min^{-1}. (b) ϕ = 6 l·min^{-1}, p = 1100 hPa and T_{sat} = -94 °C. Peak-to-peak amplitude = 33.6 ml·min^{-1}, mean value = 6.00 l·min^{-1}, standard deviation = 4.6 ml·min^{-1}. Flow rates are at pressure

As mentioned in section 2, the saturation temperature T_{sat} was estimated by means of the readings of the SPRT hosted in the saturator outlet tubing, while a second PRT immersed into the liquid bath close to the saturator, was used for estimating the saturator bath temperature T_{bath}. In thermal equilibrium conditions, these two temperatures are expected to agree within their measurement uncertainty. It should be noted that for the calculation of the water vapour amount fraction, only the saturation temperature T_{sat} has been used, since it is more representative than T_{bath} to define the water vapour saturation conditions.

In Figure 4 an example of the repeatability and stability of T_{sat}, T_{bath} and p as a function of the flow rate ϕ is shown. Over the whole investigated range, the repeatability and stability of the saturation temperature T_{sat}, expressed as peak-to-peak amplitude, resulted lower than 10 mK with a standard deviation of 1.5 mK while for the saturator bath temperature T_{bath} it resulted lower than 20 mK with a standard deviation of 3 mK.

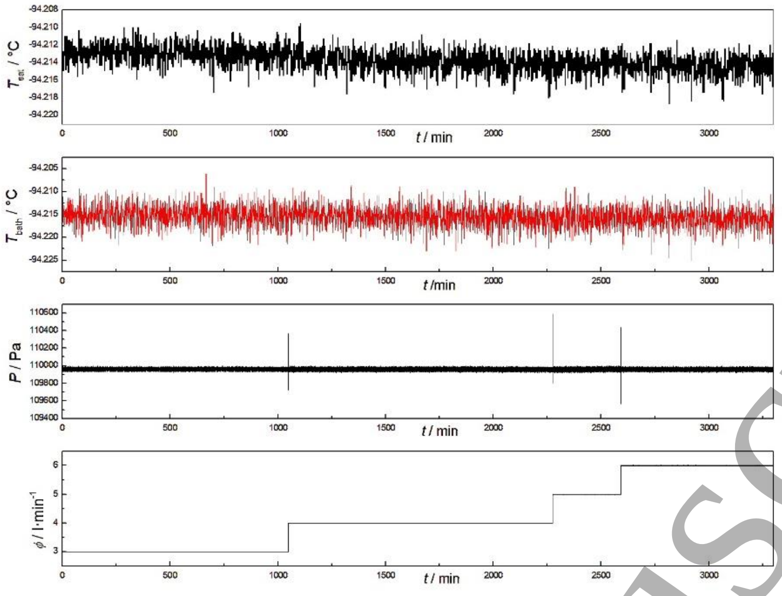

Figure 4: Stability of the water vapour saturation temperature T_{sat} and saturator bath temperature T_{bath} at a nominal temperature of -94 °C, pressure of 1100 hPa and flow rate ϕ between 3 l·min^{-1} and 6 l·min^{-1}. The temperature difference between T_{sat} and T_{bath} is lower than 3 mK.

The saturator temperature uniformity has been investigated at different saturation temperatures by vertically moving the bath PRT in a depth range of 150 mm to encompass the height of the saturator, resulting in an estimated temperature uniformity of better than 5 mK. Further, when the bath PRT and the saturation SPRT were at the same depth, T_{sat} and T_{bath} agreed to better than 5 mK over the whole temperature range.

4.2 Saturator efficiency

The evaluation of the saturator efficiency has been performed using two different approaches. The first approach consisted in detecting the change in x_{w} at the generator outlet as a function of the gas flow rate at the generation pressure. With this method, the saturator efficiency has been estimated from the difference between the reference (calculated) value of the water vapour amount fraction, $x_{\mathrm{w\_0}}$, and the readings of the CRDS analyser, $x_{\mathrm{w\_CRDS}}$, at increasing flow rates. The change in the above difference was estimated with respect to the value at the lowest flow rate, thus assuming that at the lowest flow rate the gas was fully saturated. The flow rate was varied approximately between 1 l·min^{-1} and 5 l·min^{-1}, at different working pressures, i.e. from 1 l·min^{-1} to 1.5 l·min^{-1} at 200 hPa and from 1.5 l·min^{-1} to 5 l·min^{-1} at 500 hPa, 800 hPa and 1100 hPa. The quantity $x_{\mathrm{w\_0}}$ has been determined from the measurement of T_{sat} and p through the Eq. (1). Figure 5 reports an example of the measured water vapour amount fraction $x_{\mathrm{w\_CRDS}}$ at saturation temperature and pressure of -95.2

°C and 800 hPa, respectively, that corresponds to an amount of water fraction of 45.7 nmol·mol^{-1}. Figure 6 summarises the results of the difference between $x_{\mathrm{w\_0}}$ and $x_{\mathrm{w\_CRDS}}$ as reported in Figure 5 (panel a) and those found in a further test at a saturation temperature of about -75 °C and a pressure of 1100 hPa (panel b) with respect to the difference estimated, in these specific cases, at 1.5 l·min^{-1}. The corresponding error bars, determined as the square root of the sum of the variances of the instrument readings at the current and reference flow rate conditions, are also shown. In order to get a 1 % or lower change in x_{w}, Figure 6a suggests that the maximum flow rate at -95 °C and 800 hPa should be restrained to 4 l·min^{-1}.

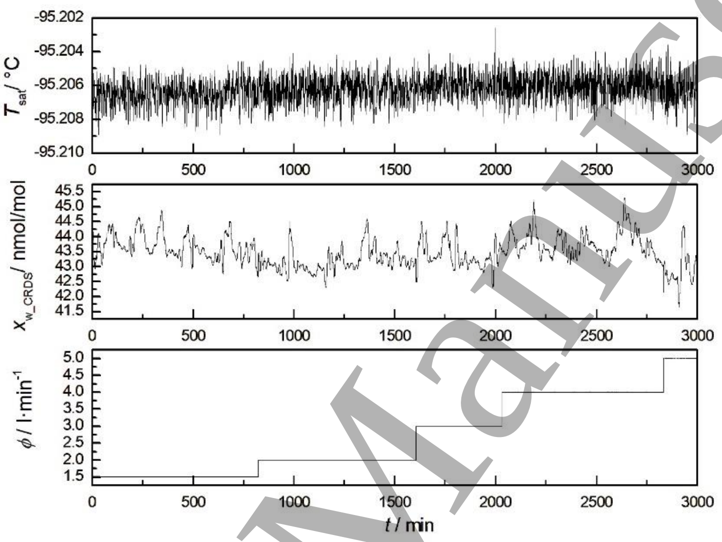

Figure 5: Water vapour amount fraction as measured by the CRDS, $x_{\mathrm{w\_CRDS}}$, as a function of the flow rate, ϕ, that ranges between 1.5 l min^{-1} and 5 l min^{-1}at operating pressure. The saturation temperature, T_{sat} is shown in the same time interval. The experiment was carried out at an absolute gas pressure of 800 hPa.

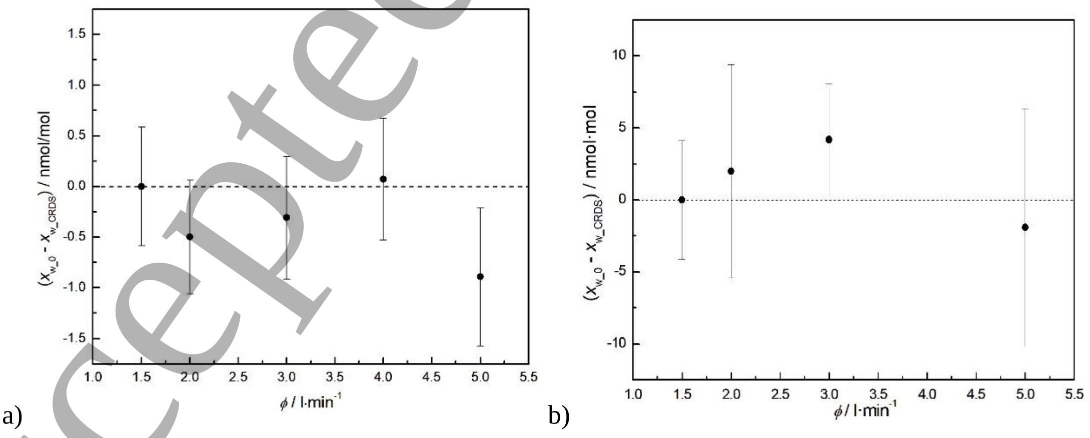

a) b)

Figure 6: Differences between the reference (calculated) value of the water vapour mole fraction $x_{\mathrm{w\_0}}$, and the water vapour mole fraction as measured by the CRDS analyser, $x_{\mathrm{w\_CRDS}}$, at several flow rates, using 1.5 l·min^{-1}as the reference flow rate. Reported data refer to: a) an absolute gas pressure of 800 hPa and a saturation temperature of -95.2 °C that corresponds to an amount fraction $x_{\mathrm{w\_0}}$ of about 45.7 nmol·mol^{-1}; b) an absolute gas pressure of 1100 hPa and a saturation

temperature of -74.9 °C that corresponds to an amount fraction x_{w_0} of about 1140 nmol·mol^{-1}. Error bars correspond to the square root of the sum of the variances of the instrument readings at the current and reference flow rate conditions.

The second approach employed for the evaluation of the saturator efficiency consisted in alternating the inlet gas between a dry source and a moist gas source. In this way the capability of the generator to saturate the carrier gas (or condensate the excess water) at the corresponding saturation temperature was assessed. In normal operation, the generator works with a nitrogen source obtained by evaporation of liquid nitrogen and further dried by molecular sieves filters to reduce the amount of water to a frost point well below -100 °C (the actual amount fraction was estimated to be 1 ppb). Bypassing the filters, the humid nitrogen gas at the saturator inlet would be characterised by a frost point temperature of about -66 °C at 0.6 MPa (corresponding to an amount of water fraction of about 800 ppb) and the saturator would work in condensation mode.

Figure 7 reports the water vapour amount fraction x_{w_CRDS} as measured by the CRDS analyser at different temperatures and pressures while the inlet gas is alternated between a dry and a humid source. Figure 7 provides a sample of the test results at two amount fractions (approximately 500 ppb and 1200 ppb) and two pressures (500 hPa and 1100 hPa). In each panel, the following quantities are given from the top to the bottom: the saturation temperature, the water vapour amount fraction x_{w_CRDS}, the mean and the standard deviations of x_{w_CRDS} and the absolute pressure p while alternating the dry and the humid nitrogen source. It is worth noting that bypassing the drying filters, the stability of the pressure is affected but the water vapour amount fraction detected by the CRDS analyser is unaffected. The temperature spikes in T_{sat} and consequently in x_{w_CRDS} were due to the autoventing control of the temperature bath that hosts the saturator.

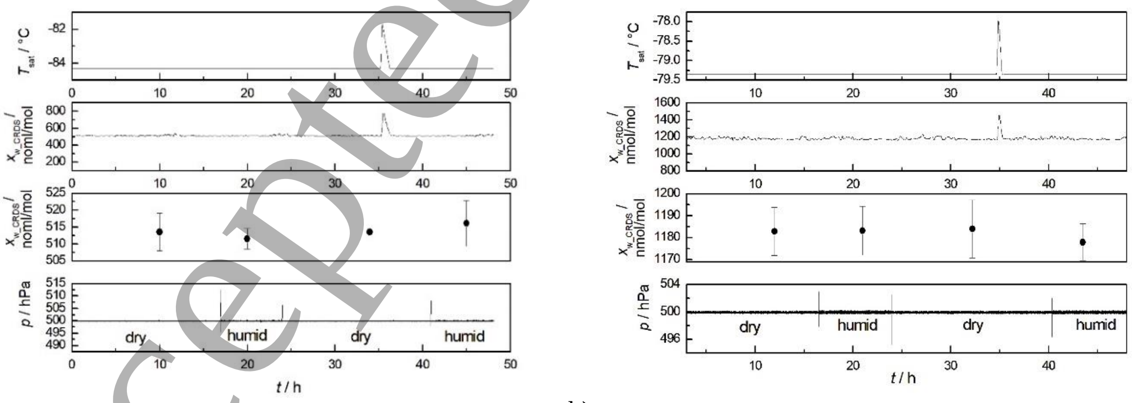

a) b)

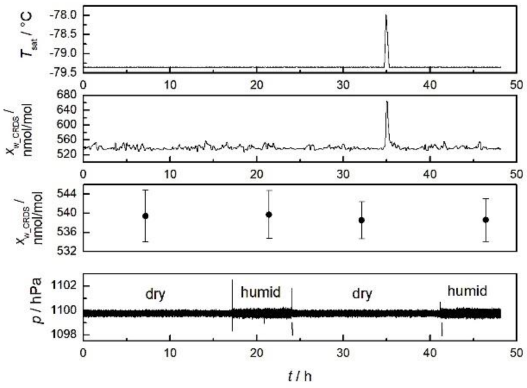

c)

Figure 7: Saturation temperature T_{sat}, water vapour amount fraction x_{w_CRDS}, mean and standard deviations of x_{w_CRDS} and absolute pressure p while alternating the inlet gas between dry (x_w < 1 nmol·mol^{-1}) and humid (x_w > 400 nmol·mol^{-1}) nitrogen. Panel a) T_{sat} = -84 °C and p = 500 hPa, b) T_{sat} = -79 °C and p =500 hPa, c) T_{sat} = -79 °C and p =1100 hPa.

4.3 Response time

Additional tests have been carried out to evaluate the INRIM 03 performance in operation. One of them consisted in changing the saturator bath temperature, and correspondingly T_{sat}, in large discrete steps and observing the response time in terms of water vapour amount fraction at the outlet of the humid gas generator. A comparison between the water vapour amount fraction, as measured by the CRDS (red line), and the reference value, as calculated from the measurement of the saturation temperature and pressure (black line) is shown in Figure 8 for a step change of T_{sat} between -95 °C and -90 °C (Figure 8a) and between -85 °C and -80 °C (Figure 8b). In both cases the tests have been carried out with a constant flow rate at 2 l·min^{-1} as well as a constant pressure at 1000 hPa.

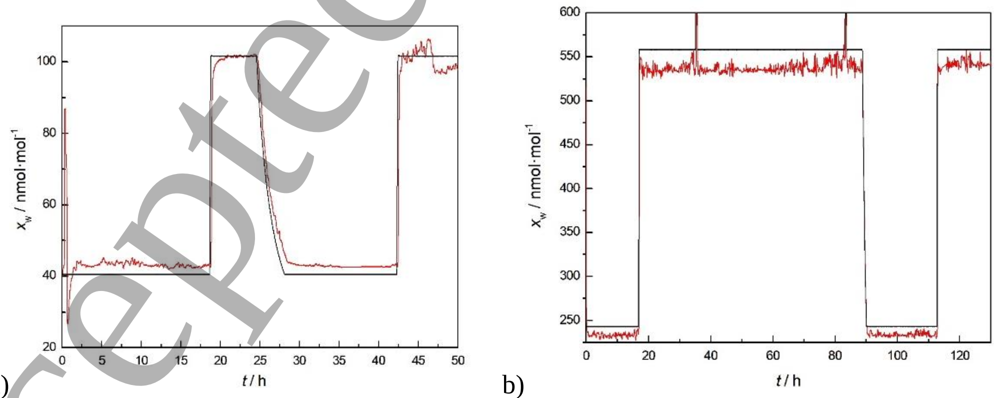

a) b)

Figure 8: Response of the humidity generator at step changes of the saturation temperature; (a) between -95 °C and -90 °C (that is, between 40 ppb and 100 ppb) and (b) between -85 °C and -80 °C (that is, between 240 ppb and 550 ppb). Measurements have been carried out at 2 l·min^{-1} at a pressure of 1000 hPa. The red line represents the water vapour

amount fraction measured by the CRDS, x_{w_CRDS}; the black line represents the reference water vapour amount fraction x_{w_0} estimated from the measurement of T_{sat} and p.

Figure 8 highlights how the measured water vapour amount fraction of the gas at the exit of the generator follows without significant delays the reference value x_w, implying a satisfactory time alignment between the generated saturation temperature and the calculated amount fraction.

Likewise, the response of the generator is even faster by varying the gas pressure. Figure 9 depicts the results obtained by maintaining a constant saturation temperature and changing the pressure between 200 hPa and 1100 hPa in steps. The test has been performed at two different saturation temperatures, that is at -95 °C and -80 °C, at a constant flow rate at pressure of 2 l·min^{-1} for all pressures but 200 hPa. To reach 200 hPa the flow rate has been decreased to 1.2 l·min^{-1} due to limitation in the pumping speed and throughput of the vacuum pump. The tests at T_{sat} = -95 °C encompassed an amount water fraction interval from 35 ppb to 190 ppb, while the test at T_{sat} = -80 °C encompassed an amount water fraction interval from 500 ppb to 2750 ppb.

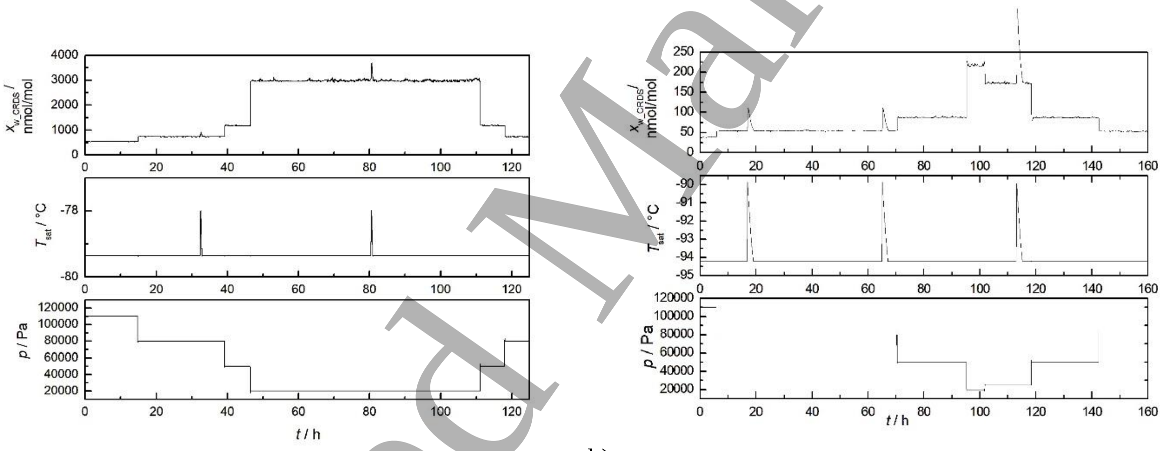

a) b)

Figure 9: Response of the humidity generator at step changes of the saturation pressure between 1100 hPa and 200 hPa. The saturation temperature has been maintained at a constant value of (a) -80 °C and (b) -95 °C.

4.4 Adsorption/desorption effects

In a trace humidity generator, the unit under calibrations are generally connected to the outlet by means of EP-SS tubing to minimise the water adsorption/desorption effects on the metal inner surface. As the humid gas passes through the pipe, the water vapour concentration may undergo fluctuations due to the adsorption and desorption of the water molecules that may occur on the internal walls of the pipe. Therefore, a comprehensive evaluation of the humidity generator performance calls for an investigation of these phenomena, particularly in the trace humidity domain, where the amount of water vapour that can be adsorbed/desorbed may represent a significant fraction of the overall water molecule concentration in the gas mixture.

In a first set of experiments, the CRDS analyser was connected to the generator by means of a heated EP-SS tubing and a shutoff diaphragm valve. The tube was kept at a constant temperature by means of a heater wrapped around it and further covered by a thermal insulation layer. This investigation was carried out by measuring the water amount fraction at the point of use with a CRDS analyser ($x_{\mathrm{w\_CRDS}}$) while heating the outlet tubing up to 110 °C until the desorption peak reversed and then cooling it down to ambient temperature. The experiment has been repeated at different saturation temperatures. Figure 10 shows some examples of the evolution of the water vapour amount fraction readings from the CRDS before and after heating the outlet pipe. The steep transition in the CRDS readings in Figure 10 corresponds to the time when the tubing temperature approaches 100 °C.

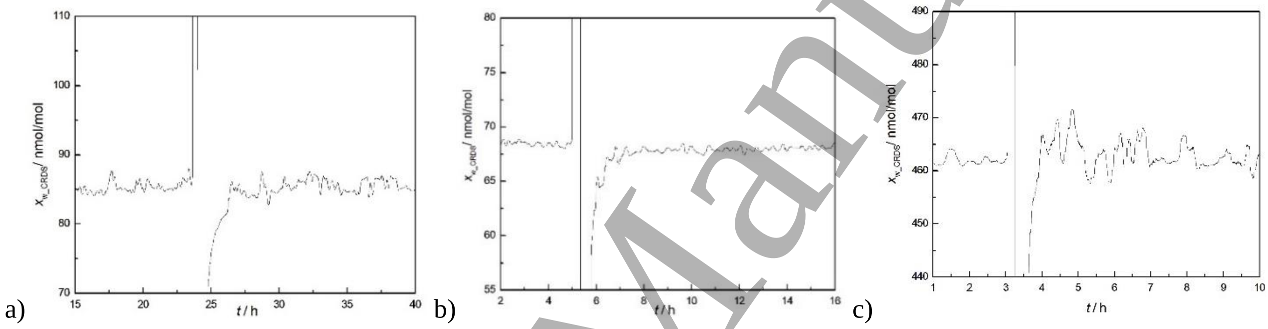

Figure 10: Adsorption/desorption effects of water vapour on the inner surface of the generator outlet EP-SS tubing detected through the measurement of the water vapour amount fraction, $x_{\mathrm{w\_CRDS}}$, before and after heating the outlet pipe, in the following conditions: a) T_{sat} = -99 °C, p = 200 hPa, ϕ =1.5 l·min^{-1} ; b) T_{sat} = -94 °C, p = 500 hPa, ϕ =2 l·min^{-1}; c) T_{sat} = -80 °C, p =1100 hPa , ϕ =2 l·min^{-1}.

As expected, when the tubing was heated up water molecules started to desorb from the inner tube surface. The plots show the transient phenomena with an overshoot, associated with the rapid increase in the water vapour concentration, and a subsequent undershoot of the CRDS reading. It can be noted that after the transient, at least 8 hours were needed to recover a steady-state condition, with an even longer time in case of lower water vapour concentrations. The difference between the average water vapour amount fraction measured before and after the transient heating in the three experiments, as showed in Figure 10, were a) 0.11 nmol·mol^{-1} or 0.12 % of the reading, b) 0.56 nmol·mol^{-1} or 0.8 % of the reading, and c) 0.38 nmol·mol^{-1} or 0.08 % of the reading, respectively.

In a second set of experiments, the transient behaviour of the system as a result of stepping the saturation temperature up and down as shown in Figure 8a and 8b has been analysed. An evaluation of the adsorption/desorption transient effects has been obtained by comparing the measured water vapour concentration before and after the saturation temperature steps. Figure 11 shows examples of zoomed sections of Figure 8 where the red line represents the measured water vapour amount fraction, $x_{\mathrm{w\_CRDS}}$, while the black line is the calculated reference value, $x_{\mathrm{w\_0}}$. Although a step change in $x_{\mathrm{w\_0}}$ is comparatively fast, the $x_{\mathrm{w\_CRDS}}$ reading takes a much longer time to recover a steady-state condition. The overall recovery time is associated with the phenomena of water molecules desorption or absorption in the system which occur when the water vapour concentration decreases (T_{sat} decreases) or increases (T_{sat} increases), respectively.

The above experiments were carried out over the whole temperature and pressure range at low flow rates (1.5 l/min at 200 hPa, 2 l/min at 1100 hPa). It was a worst-case estimate of the measurement uncertainty associated with the adsorption/desorption effects, as a higher flow rate would dilute the desorbed water and reduce its impact. In the following Section 5.1, the results will be further discussed.

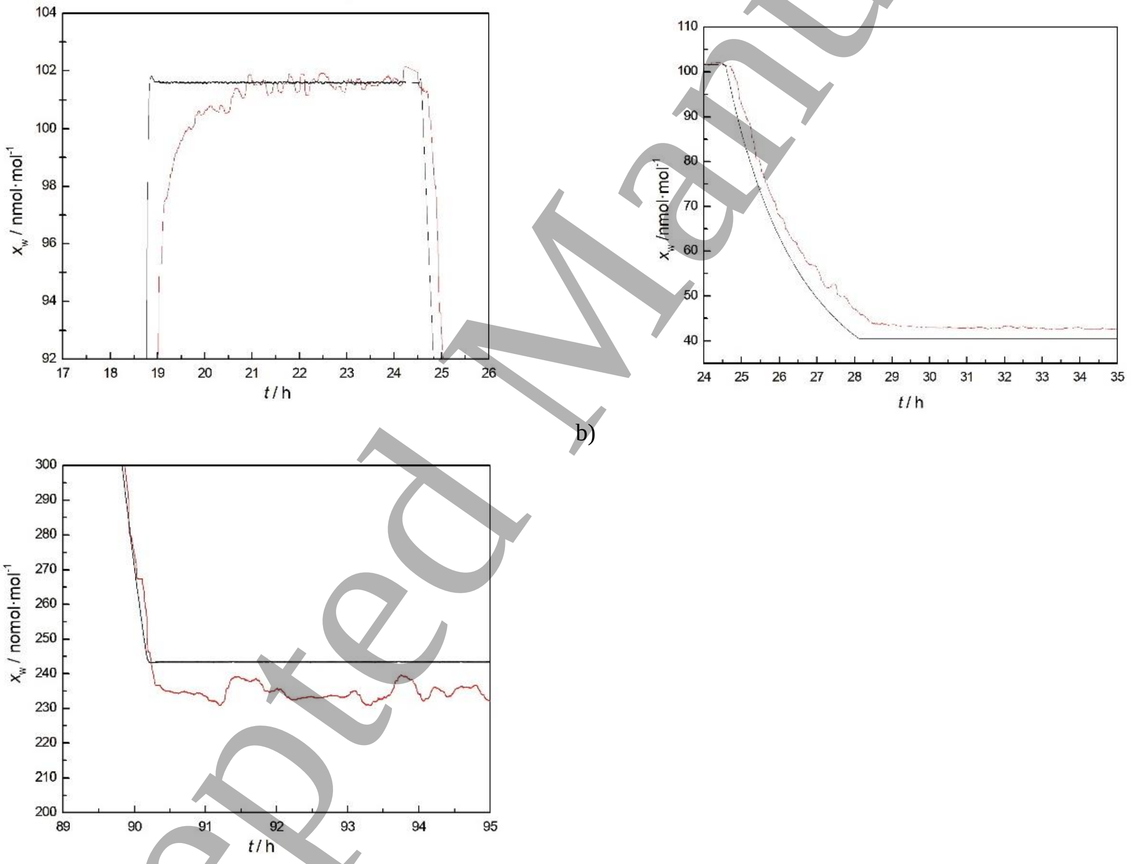

a)

b)

c)

Figure 11: Effects of the water molecules desorption and absorption phenomena on the water vapour amount fraction detected by the CRDS analyser. The red line is the measured amount of water fraction $x_{\mathrm{w\_CRDS}}$, while the black line is the calculated reference value $x_{\mathrm{w\_0}}$.

5. Evaluation of the measurement uncertainty

The measurement uncertainty for the water vapour amount fraction x_w, and the frost-point temperature T_{fp}, of the humid gas generated by the INRIM 03 has been evaluated in the temperature range between -75 °C and -100 °C and in the pressure range between 200 hPa and 1100 hPa. Such an evaluation took into account the result of the experiments discussed in this work, together with the uncertainty of the formulations of the enhancement factor and of the saturation vapour pressure along the sublimation line (i.e., the equilibrium of ice and its water vapour).

The detailed uncertainty contributions considered for the estimation of the measurement uncertainty of T_{fp}, p and x_w are reported in the tables in Appendix B. By way of example, the following four tables are given below: Tables 1 reports the uncertainty budget for T_{fp} = -75 °C at p = 1100 hPa; Tables 2reports the uncertainty budget for T_{fp} = -75 °C at p = 200 hPa; Tables 3 reports the uncertainty budgets for T_{fp} = -100 °C at p = 1100 hPa; and Tables 4 reports the uncertainty budgets for T_{fp} = -100 °C at p = 200 hPa.

Tables 1-to-4 report the sources of uncertainty for each quantity under investigation together with the corresponding standard uncertainty, the associated probability distribution function (PDF) and the sensitivity coefficient. The last column reports the estimated standard uncertainty that contributes to the combined uncertainty, whose numerical value comes from the product of the input standard uncertainty by the relevant sensitivity coefficient. Finally, the combined standard uncertainty associated with the measurand, either T_{fp}, p or x_w, have been estimated as the square root of the input variances, by assuming that no correlation exists among the individual uncertainty sources.

Table 1: INRIM 03 uncertainty budget for the frost-point temperature, T_{fp}, pressure, p, and water vapour amount fraction, x_w at the following nominal values: T_{fp} = -75 °C, p = 1100 hPa and x_w=1118 nmol·mol^{-1}.

T_{fp} = -75 °C p = 1100 hPa x_w = 1118 nmol·mol^{-1}				
Uncertainty budget for T_{fp} / °C				
Source of uncertainty	Standard uncertainty	PDF	Sensitivity coefficient	Contribution to combined uncertainty/°C
Saturation temperature repeatability	0.00088 °C	Normal	1	$8.8\cdot10^{-4}$
Saturator temperature uniformity	0.000086 °C	Rectangular	1	$8.6\cdot10^{-4}$
SPRT calibration	0.00025 °C	Normal	1	$2.5\cdot10^{-4}$
Temperature resistance bridge accuracy	0.00043 °C	Rectangular	1	$4.3\cdot10^{-4}$
SPRT drift	0.0017 °C	Rectangular	1	$1.7\cdot10^{-3}$
Self-heating SPRT	0.00066 °C	Asym. Triangular	1	$1.6\cdot10^{-4}$
Adsorption/Desorption	0.034 °C	Normal	1	$3.4\cdot10^{-2}$

Saturation efficiency	0.0068 °C	Rectangular	1	$6.8\cdot10^{-3}$
Combined standard uncertainty, $u_c(T_{fp})$ / °C				**0.034**

Uncertainty budget for p /Pa

Source of uncertainty	Standard uncertainty	PDF	Sensitivity coefficient	Contribution to combined uncertainty/Pa
Pressure control stability	5.4 Pa	U-distribution	1	5.4
Transducer calibration	3.3 Pa	Normal	1	3.3
Long term stability	15.1 Pa	Rectangular	1	15.1
Linearity and temperature effects	7.6 Pa	Rectangular	1	7.6
Resolution	0.03 Pa	Rectangular	1	0.03
Combined standard uncertainty, $u_c(p)$ / Pa				**18.0**

Uncertainty budget for x_w /mol·mol^{-1}

Source of uncertainty	Standard uncertainty	PDF	Sensitivity coefficient	Contribution to combined uncertainty/ mol·mol^{-1}
Saturation pure water vapour pressure, $e(T_{fp})$	0.0002 Pa	Normal	$9.18\cdot10^{-6}$ Pa^{-1}	$2.15\cdot10^{-9}$
Enhancement factor, $f(T_{fp},p)$	0.0005	Normal	$1.13\cdot10^{-6}$	$5.65\cdot10^{-10}$
Frost point temperature, T_{fp}	0.034 °C	Normal	$1.80\cdot10^{-7}$ °C^{-1}	$6.19\cdot10^{-9}$
Pressure, p	18.0 Pa	Normal	$1.71\cdot10^{-12}$ Pa^{-1}	$3.09\cdot10^{-11}$
Combined standard uncertainty, $u_c(x_w)$ / mol·mol^{-1}				**$6.58\cdot10^{-9}$**
Percent relative standard uncertainty, $100\cdot u_c(x_w)$ / x_w				**0.59**

Table2: INRIM 03 uncertainty budget for the frost-point temperature, T_{fp}, pressure, p, and water vapour amount fraction, x_w at the following nominal values: T_{fp} = -75 °C, p = 200 hPa and x_w= 6104 nmol·mol^{-1}.

T_{fp} = -75 °C p = 200 hPa x_w = 6104 nmol·mol^{-1}

Uncertainty budget for T_{fp} / °C

Source of uncertainty	Standard uncertainty	PDF	Sensitivity coefficient	Contribution to combined uncertainty / °C
Saturation temperature repeatability	0.00077 °C	Normal	1	$7.7\cdot10^{-4}$
Saturator temperature uniformity	0.00028 °C	Rectangular	1	$2.8\cdot10^{-4}$
SPRT calibration	0.00025 °C	Normal	1	$2.5\cdot10^{-4}$
Temperature resistance bridge accuracy	0.00043 °C	Rectangular	1	$4.3\cdot10^{-4}$
SPRT drift	0.0017 °C	Rectangular	1	$1.7\cdot10^{-3}$
Self-heating SPRT	0.00066 °C	Asym. Triangular	1	$1.6\cdot10^{-4}$
Adsorption/Desorption	0.032 °C	Normal	1	$3.2\cdot10^{-2}$
Saturation efficiency	0.00082 °C	Rectangular	1	$8.2\cdot10^{-4}$
Combined standard uncertainty, $u_c(T_{fp})$ / °C				**0.032**

Uncertainty budget for p /Pa				
Source of uncertainty	Standard uncertainty	PDF	Sensitivity coefficient	Contribution to combined uncertainty / Pa
Pressure control stability	3.7 Pa	U-distribution	1	3.7
Transducer calibration	2.0 Pa	Normal	1	2.0
Long term stability	15.1 Pa	Rectangular	1	15.1
Linearity and temperature effects	7.6 Pa	Rectangular	1	7.6
Resolution	0.03 Pa	Rectangular	1	0.03
Combined standard uncertainty, $u_c(p)$ /Pa				**17.4**

Uncertainty budget for x_w /mol·mol^{-1}				
Source of uncertainty	Standard uncertainty	PDF	Sensitivity coefficient	Contribution to combined uncertainty/ mol·mol^{-1}
Saturation pure water vapour pressure, $e(T_{fp})$	0.00024 Pa	Normal	$5.01\cdot10^{-5}$ Pa^{-1}	$1.18\cdot10^{-8}$
Enhancement factor, $f(T_{fp},p)$	0.000087	Normal	$6.21\cdot10^{-6}$	$5.39\cdot10^{-10}$
Frost point temperature, T_{fp}	0.032 °C	Normal	$9.74\cdot10^{-7}$ °C^{-1}	$3.12\cdot10^{-8}$
Pressure, p	17.4 Pa	Normal	$2.64\cdot10^{-10}$ Pa^{-1}	$4.59\cdot10^{-9}$
Combined standard uncertainty, $u_c(x_w)$ / mol·mol^{-1}				**$3.37\cdot10^{-8}$**
Percent relative standard uncertainty, $100\cdot u_c(x_w)$ / x_w				**0.55**

Table 3: INRIM 03 uncertainty budget on the frost-point temperature, T_{fp}, pressure, p, and water vapour amount fraction, x_w at the following nominal values: T_{fp} = -100 °C, p = 1100 hPa and x_w= 13 nmol·mol^{-1}.

T_{fp} = -100 °C p = 1100 hPa x_w = 13 nmol·mol^{-1}				
Uncertainty budget for T_{fp} / °C				
Source of uncertainty	Standard uncertainty	PDF	Sensitivity coefficient	Contribution to combined uncertainty / °C
Saturation temperature repeatability	0.0017 °C	Normal	1	$1.7\cdot10^{-3}$
Saturator temperature uniformity	0.00049 °C	Rectangular	1	$4.9\cdot10^{-4}$
SPRT calibration	0.00025 °C	Normal	1	$2.5\cdot10^{-4}$
Temperature resistance bridge accuracy	0.00043 °C	Rectangular	1	$4.3\cdot10^{-4}$
SPRT drift	0.0017 °C	Rectangular	1	$1.7\cdot10^{-3}$
Self-heating SPRT	0.00066 °C	Asym. Triangular	1	$1.6\cdot10^{-4}$
Adsorption/Desorption	0.025 °C	Normal	1	$2.5\cdot10^{-2}$
Saturation efficiency	0.13 °C	Rectangular	1	$1.3\cdot10^{-1}$
Combined standard uncertainty, $u_c(T_{fp})$ / °C				**0.131**
Uncertainty budget for p /Pa				
Source of uncertainty	Standard uncertainty	PDF	Sensitivity coefficient	Contribution to combined uncertainty/ Pa

Pressure control stability	6.0 Pa	U-distribution	1	6.0
Transducer calibration	3.1 Pa	Normal	1	3.1
Long term stability	15.1 Pa	Rectangular	1	15.1
Linearity and temperature effects	7.6 Pa	Rectangular	1	7.6
Resolution	0.03 Pa	Rectangular	1	0.03
Combined standard uncertainty, $u_c(p)$ / Pa				**18.2**

Uncertainty budget for x_w /mol·mol^{-1}

Source of uncertainty	Standard uncertainty	PDF	Sensitivity coefficient	Contribution to Standard uncertainty/ mol·mol^{-1}
Saturation pure water vapour pressure, $e(T_{fp})$	0.0000048 Pa	Normal	$9.19\cdot10^{-6}$ Pa^{-1}	$4.45\cdot10^{-11}$
Enhancement factor, $f(T_{fp},p)$	0.00071	Normal	$1.55\cdot10^{-8}$	$1.10\cdot10^{-11}$
Frost point temperature, T_{fp}	0.131 °C	Normal	$3.20\cdot10^{-9}$ °C^{-1}	$4.18\cdot10^{-10}$
Pressure, p	18.2 Pa	Normal	$1.14\cdot10^{-14}$ Pa^{-1}	$2.08\cdot10^{-13}$
Combined standard uncertainty, $u_c(x_w)$ / mol·mol^{-1}				**$4.21\cdot10^{-10}$**
Percent relative standard uncertainty, $100\cdot u_c(x_w)$ / x_w				**3.24**

Table 4: INRIM 03 uncertainty budget on the frost-point temperature, T_{fp}, pressure, p, and water vapour amount fraction, x_w at the following nominal values: T_{fp} = -100 °C, p = 200 hPa and x_w= 70 nmol·mol^{-1}.

T_{fp} = -100 °C p = 200 hPa x_w = 70 nmol·mol^{-1}

Uncertainty budget for T_{fp} / °C

Source of uncertainty	Standard uncertainty	PDF	Sensitivity coefficient	Contribution to combined uncertainty/ °C
Saturation temperature repeatability	0.0014 °C	Normal	1	$1.4\cdot10^{-3}$
Saturator temperature uniformity	0.00024 °C	Rectangular	1	$2.4\cdot10^{-4}$
SPRT calibration	0.00025 °C	Normal	1	$2.5\cdot10^{-4}$
Temperature resistance bridge accuracy	0.00043 °C	Rectangular	1	$4.3\cdot10^{-4}$
SPRT drift	0.0017 °C	Rectangular	1	$1.7\cdot10^{-3}$
Self-heating SPRT	0.00066 °C	Asym. Triangular	1	$1.6\cdot10^{-4}$
Adsorption/Desorption	0.025 °C	Normal	1	$2.5\cdot10^{-2}$
Saturation efficiency	0.0061	Rectangular	1	$6.1\cdot10^{-3}$
Combined standard uncertainty, $u_c(T_{fp})$ / °C				**0.026**

Uncertainty budget for p /Pa

Source of uncertainty	Standard uncertainty	PDF	Sensitivity coefficient	Contribution to combined uncertainty/ Pa
Pressure control stability	3.2 Pa	U-distribution	1	3.2

Transducer calibration	2.0 Pa	Normal	1	2.0
Long term stability	15.1 Pa	Rectangular	1	15.1
Linearity and temperature effects	7.6 Pa	Rectangular	1	7.6
Resolution	0.03 Pa	Rectangular	1	0.03
Combined standard uncertainty, $u_c(p)$ / Pa				**17.3**
Uncertainty budget for x_w /mol·mol^{-1}				
Source of uncertainty	Standard uncertainty	PDF	Sensitivity coefficient	Contribution to combined uncertainty/ mol·mol^{-1}
Saturation pure water vapour pressure, $e(T_{fp})$	0.0000048 Pa	Normal	$5.00\cdot10^{-5}$ Pa^{-1}	$2.43\cdot10^{-10}$
Enhancement factor, $f(T_{fp},P)$	0.00013	Normal	$8.51\cdot10^{-8}$	$1.10\cdot10^{-11}$
Frost point temperature, T_{fp}	0.026 °C	Normal	$1.72\cdot10^{-8}$ °C^{-1}	$4.41\cdot10^{-10}$
Pressure, p	17.3 Pa	Normal	$3.42\cdot10^{-12}$ Pa^{-1}	$5.92\cdot10^{-11}$
Combined standard uncertainty, $u_c(x_w)$ / mol·mol^{-1}				**$5.07\cdot10^{-10}$**
Percent relative standard uncertainty, $100\cdot u_c(x_w)$ / x_w				**0.72**

5.1 Estimate of adsorption/desorption and saturator efficiency uncertainties

As Tables 1-to-4 highlight, the adsorption/desorption effect and the saturation efficiency represent the main sources of uncertainty to frost-point temperature measurement uncertainty. The adsorption/desorption effect contribution has been estimated in the experiments described in section 4.4 based on water vapour amount fraction measurements carried out with a commercial CRDS analyser. The analyser used in these experiments showed a measurement repeatability of 0.5 % or 0.5 ppb, whichever is greater, thus limiting our capability in characterising the humidity generator at the lowest frost point temperatures. In fact, Table 5 shows the impact of the repeatability of amount fraction measurements on the corresponding frost-point temperature measurements.

Table 5: The impact of the repeatability Δx_w of a CRDS analyser measurement (measuring in amount of water fraction unit) on the repeatability ΔT_{fp} of frost point temperature measurements (see text). The CRDS measurement repeatability is 0.5 % or 0.5 ppb, whichever is greater. The nominal T_{fp} has been calculated at p = 1000 hPa.

x_w /ppb	Δx_w /ppb		ΔT_{fp} /°C	T_{fp} /°C
1000	5	→	0.03	-76.3
100	0.5	→	0.03	-89.9
50	0.5	→	0.06	-93.6
20	0.5	→	0.12	-98.3

The differences between the water vapour amount fraction measured: *i)* before and after the heating of the generator outlet pipe; *ii)* before and after the increase and decrease of T_{sat}; and *iii)* before and after the decrease and increase of T_{sat} are shown as percent relative differences $100 \cdot \Delta x_w / x_w$ as a function of x_w in Figure 12. For each data point, the corresponding relative uncertainty bar is also reported. A weighted least-squared linear fitting to all data points resulted in a very small angular coefficient of the fitting line ($b \cong -3 \cdot 10^{-4}$ nmol^{-1}·mol); in the limiting case of an angular coefficient equal to zero, it could be concluded that the quantity $\Delta x_w / x_w$ would be constant with x_w. To estimate the uncertainty associated with the adsorption/desorption effect, it was assumed the quantity $\Delta x_w / x_w$ be constant and normally-distributed about zero with a worst-case confidence limit at 95 % (k = 2) equal to 1.05 %.

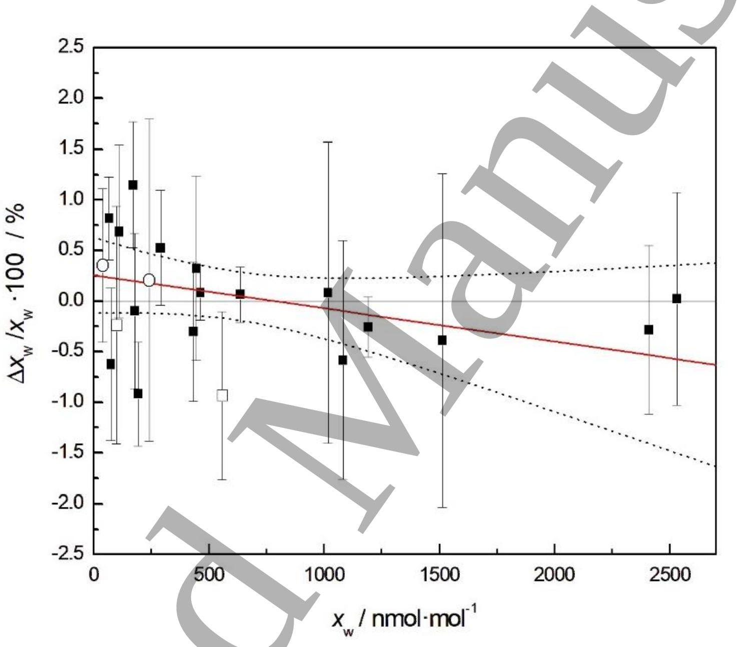

Figure 12: Percentage relative differences $100 \cdot \Delta x_w / x_w$, as a function of x_w, between the water vapour amount fraction as measured before and after the heating of the generator outlet pipe (■); before and after the increase and decrease of T_{sat} (○); before and after the decrease and increase of T_{sat} (□). The estimated coefficients of the linear regression equation $\Delta x_w / x_w = a + b \cdot x_w$ and their standard uncertainties are: $a = (0.26 \pm 0.18)$ and $b = (-3.28 \pm 2.20) \cdot 10^{-4}$ nmol^{-1}·mol. Regression line (—). Upper and lower 95 % confidence limits (---).

In terms of frost-point temperature, the adsorption/desorption effect contributes to the whole uncertainty for a quantity of about 0.034 °C at T_{fp} = -75 °C and 0.025 °C at T_{fp} = -100 °C.

The saturator efficiency contribution to the frost-point temperature uncertainty has been determined according to both approaches described in section 4.2. In the first approach, for each combination of p and T_{sat}, the saturator efficiency has been estimated by considering a rectangular probability distribution with a width equal to the maximum difference between the reference (calculated) x_{w_0}, and the corresponding measurement with the CRDS analyser $x_{\mathrm{w\_CRDS}}$ as a function of the gas flow rate. In the second approach, the mean and the standard deviations of $x_{\mathrm{w\_CRDS}}$ was estimated for each combination of p and T_{sat}, while alternating a dry source and a moist nitrogen source, to assess the capability of the saturator to saturate the carrier gas (or condensate the excess water). The worst-case estimates (i.e. 0.0068 °C at T_{fp} = -75 °C, p = 1100 hPa; 0.00082 °C at T_{fp} = -75 °C, p = 200 hPa; 0.13 °C at T_{fp} = -100 °C, p = 1100 hPa; 0.025 °C at T_{fp} = -100 °C, p = 200 hPa) were selected and reported in the Tables 1-to-4.

5.2 Temperature stability and uniformity

Concerning the other sources of uncertainty, a Type A evaluation of the measurement uncertainty associated to the saturation temperature repeatability has been estimated from the standard deviation of repeated measurements of T_{sat} assuming a normally-distributed quantity, while the uncertainty contribution due to the temperature uniformity has been evaluated by vertically moving the bath PRT along the height of the saturator, wherein the maximum temperature difference corresponds to the full width of a symmetric rectangular probability distribution. The contributions of the saturation temperature repeatability and of the temperature uniformity to the whole uncertainty budget are estimated to be respectively: 0.00088 °C and 0.000086 °C at T_{fp} = -75 °C, p = 1100 hPa; 0.00077 °C and 0.00028 °C at T_{fp} = -75 °C, p = 200 hPa; 0.0017 °C and 0.00049 °C at T_{fp} = -100 °C, p = 1100 hPa; 0.0014 °C and 0.00024 °C at T_{fp} = -100 °C, p = 200 hPa.

5.3 Pressure control stability

The measurement uncertainty associated to the stability of the pressure control system has been inferred from the standard deviation of repeated measurements of p, assuming a U-shaped probability distribution of pressures, because of the cyclic variation in time caused by the pressure controller. In the worst case the contribution of the pressure control stability to the whole pressure uncertainty resulted less than 7 Pa.

5.4 Estimate of the SPRT self-heating uncertainty

The SPRT excitation current causes an increase of the thermometer resistance (self-heating) due to the Joule effect: $R_0 + \Delta R = R_0 + r_\theta R I^2$ where r_θ is proportional to the thermal resistance between the thermometer and the medium. ΔR is usually estimated at the triple point of water during fixed-point calibration. However, in our application, the SPRT attain its equilibrium in a convective gas flow, in contrast with the above measurement in a liquid medium, calling for a specific assessment of ΔR. The resistance of the thermometer has been measured at 1 mA, 2 mA and 3 mA at 2 l·min^{-1} and 4 l·min^{-1} at 1100 hPa. Since in the current thermo-fluid-dynamic conditions the self-heating depends more on the flow rate than on the pressure, only its variation with respect to the flow has been investigated. Linear fitting the measured resistance versus the squared excitation current and extrapolating back to I = 0 mA allowed an estimation of the zero-current thermometer resistance R_0, while the increment of the resistance with the excitation current inferred by the angular coefficient of the fitting line is equal to $6.7 \cdot 10^{-5}$ Ω/mA^2, corresponding to a ΔR =67-μΩ self-heating for an excitation current of 1 mA. It was assumed the difference ΔR be described by an asymmetric triangular probability distribution of a random variable X, with the zero-probability lower bound corresponding to R_0 and the maximum-probability upper bound corresponding to $R_0 + \Delta R$. Given such an asymmetric triangular PDF, the expected self-heating correction resulted in $E[X] = \Delta R/3$ with a standard uncertainty equal to $u[X] = \Delta R/(3\sqrt{2})$, i.e. 0.0002 °C and 0.00016 °C respectively as reported in Tables 1-to-4.

Once the combined standard uncertainty of the frost-point temperature $u_c(T_{fp})$ and pressure $u_c(p)$ have been evaluated, the combined standard uncertainty of the reference water vapour amount fraction $u_c(x_w)$ has been determined by means of Eq. (2). A preliminary uncertainty evaluation of water vapour amount fraction and frost-point temperature for the INRIM 03 humidity generator operating at the atmospheric pressure had been already discussed in Cuccaro *et al.* [2] in the frost-point temperature range between -20 °C and -75 °C. The experiments at -75 °C and 1100 hPa of the present characterisation compares satisfactorily with the previous work. The increased uncertainty of the frost-point temperature in the current evaluation, i.e. $u_c(T_{fp})$ =0.034 °C versus $u_c(T_{fp})$ =0.014 °C reported in Cuccaro *et al.* [2], is mainly due to the uncertainty contribution of adsorption/desorption effects that had not been considered in the previous work. However, at the lowest water vapour amount fractions the uncertainty associated with the saturation efficiency represents the main contribution to the overall uncertainty budget, because of the limited performance of the CRDS moisture analyser that had been used for the current characterisation. Indeed, it is speculated that if the evaluation of the saturation efficiency had been made using a state-of-the-art CRDS analyser - with a lower detection limit and a higher measurement repeatability - such an uncertainty contribution would have been significantly smaller, especially at the lowest water vapour amount fractions.

6. Conclusions

A low frost-point humidity generator able to operate at sub-atmospheric pressure has been designed and constructed at INRIM with the aim of providing the metrological traceability both to instruments developed for the measurement of humidity in atmosphere and to sensors and analysers used in industry for controlling and measuring the amount of water vapour in manufacturing processes. The generator, named INRIM 03, covers the frost point temperature range between -100 °C and -20 °C, and operates in the pressure range between 1100 hPa and 200 hPa, corresponding to an amount of water fraction range from $13\cdot10^{-9}$ mol·mol^{-1} to $5.2\cdot10^{-3}$ mol·mol^{-1}.

In this work, a comprehensive set of tests carried out to validate the individual uncertainty components are presented along with a detailed uncertainty evaluation over the frost-point temperature range from -100 °C to -75 °C and over the water vapour amount fraction range between $13\cdot10^{-9}$ mol·mol^{-1} and $6.1\cdot10^{-6}$ mol·mol^{-1}. The current tests complement and supplement those previously reported in [2]. The results showed that in the frost-point temperature range between -75 °C and -95 °C, an expanded uncertainty (k=2) equal to 0.07 °C was found, while at -100 °C frost point the expanded uncertainty was 0.26 °C. The relative expanded uncertainty (k=2) associated with water vapour amount fraction measurements was estimated equal to or better than 1.2 % between $35\cdot10^{-9}$ mol·mol^{-1} and $6.1\cdot10^{-6}$ mol·mol^{-1}, increasing up to 6.5 % at $13\cdot10^{-9}$ mol·mol^{-1}. Based on the generator performances observed during this work, it is speculated that further improvements are possible once a suitable state-of-the-art hygrometer would be available for an even more detailed metrological characterization.

Acknowledgements

This work has been carried out within the European Metrology Programme for Innovation and Research (EMPIR) Project “PROMETH2O - Metrology for trace water in ultra-pure process gases”. This project (Grant no. 20IND06 PROMETH2O) has received funding from the EMPIR programme co-financed by the Participating States and from the European Union's Horizon 2020 research and innovation programme.

Data availability statement

The data that support the findings of this study are available upon request from the authors.

Appendix A

Derivation of the Uncertainty Equations

As introduced in Section 2, the water vapour amount fraction, x_w, at the generator gas outlet is given by the equation:

$$x_\mathrm{w} = \frac{f(T_\mathrm{sat}, p)\cdot e_\mathrm{w}(T_\mathrm{sat})}{p} \tag{A.1}$$

where $e_\mathrm{w}(T_\mathrm{sat})$ is the saturation vapour pressure over ice at the temperature T_sat, p is the total system pressure and $f(T_\mathrm{sat}, p)$ is the water vapour enhancement factor, which takes into account the non-ideal behaviour of the gas mixture.

The combined standard uncertainty, $u(x_\mathrm{w})$, is thus given by:

$$u(x_\mathrm{w}) = \sqrt{\left[x_\mathrm{w}\left(\frac{1}{f}\frac{\partial f}{\partial T_\mathrm{sat}} + \frac{1}{e_\mathrm{w}}\frac{\partial e_\mathrm{w}}{\partial T_\mathrm{sat}}\right)\right]^2 \cdot u_\mathrm{c}^2(T_\mathrm{sat}) + \left[x_\mathrm{w}\left(\frac{1}{f}\frac{\partial f}{\partial p} - \frac{1}{p}\right)\right]^2 \cdot u_\mathrm{c}^2(p) + \left(\frac{e_\mathrm{w}}{p}\right)^2 \cdot u^2(f) + \left(\frac{f}{p}\right)^2 \cdot u^2(e_\mathrm{w})} \quad , \qquad \text{(A.2)}$$

where

$u_\mathrm{c}(T_\mathrm{sat})$ and $u_\mathrm{c}(p)$ are the combined measurement uncertainties of the saturation temperature and the pressure, respectively;

$u(e_\mathrm{w})$ and $u(f)$ are the standard uncertainties of $e_\mathrm{w}(T_\mathrm{sat})$ and $f\,(T_\mathrm{sat}, p)$, respectively;

the terms

$x_\mathrm{w}\left(\frac{1}{f}\frac{\partial f}{\partial T_\mathrm{sat}} + \frac{1}{e_\mathrm{w}}\frac{\partial e_\mathrm{w}}{\partial T_\mathrm{sat}}\right)$, $x_\mathrm{w}\left(\frac{1}{f}\frac{\partial f}{\partial p} - \frac{1}{p}\right)$, $\frac{e_\mathrm{w}}{p}$ and $\frac{f}{p}$ are the relevant sensitivity coefficients.

Equation A.2 is determined applying the general law of uncertainty propagation to the equation A.1, which can be rewritten as follows:

$$x_\mathrm{w} = \frac{f\,(T_\mathrm{sat}, p, \omega) \cdot e_\mathrm{w}(T_\mathrm{sat}, \lambda)}{p} \qquad \text{(A.3)}$$

where the quantities ω and λ are introduced to take into account the uncertainties associated with the equations used to formulate the enhancement factor and the saturation vapour pressure over ice respectively [18]. The quantities ω and λ are considered as multipliers with an estimated value of 1 and an uncertainty equal to the relative uncertainty of the calculated values.

Thus λ =1 and $u(\lambda) = u_\mathrm{r}(e_\mathrm{w})$, and ω =1 and $u(\omega) = u_\mathrm{r}(f)$, where $u_\mathrm{r}(e_\mathrm{w})$ is estimated by using the formulation given by the 2011 IAPWS release for the sublimation pressure of ice *Ih* [13], while the estimation of $u_\mathrm{r}(f)$ is based on the work of Lovell-Smith [16] (see Section 2).

The total uncertainty of x_w is then determined considering the partial derivatives with respect to the relevant quantities T_sat, p, ω and λ, reported below:

$$\frac{\partial x_\mathrm{w}}{\partial T_\mathrm{sat}} = \frac{\partial x_\mathrm{w}}{\partial f} \cdot \frac{\partial f}{\partial T_\mathrm{sat}} + \frac{\partial x_\mathrm{w}}{\partial e_\mathrm{w}} \cdot \frac{\partial e_\mathrm{w}}{\partial T_\mathrm{sat}} = \frac{e_\mathrm{w}}{p} \cdot \frac{\partial f}{\partial T_\mathrm{sat}} + \frac{f}{p} \cdot \frac{\partial e_\mathrm{w}}{\partial T_\mathrm{sat}} = \frac{f \cdot e_\mathrm{w}}{p}\left(\frac{1}{f}\frac{\partial f}{\partial T_\mathrm{sat}} + \frac{1}{e_\mathrm{w}}\frac{\partial e_\mathrm{w}}{\partial T_\mathrm{sat}}\right) = x_\mathrm{w}\left(\frac{1}{f}\frac{\partial f}{\partial T_\mathrm{sat}} + \frac{1}{e_\mathrm{w}}\frac{\partial e_\mathrm{w}}{\partial T_\mathrm{sat}}\right) \qquad \text{(A.4)}$$

$$\frac{\partial x_\mathrm{w}}{\partial p} = \frac{\partial x_\mathrm{w}}{\partial f} \cdot \frac{\partial f}{\partial p} - \frac{1}{p^2} \cdot f \cdot e_\mathrm{w} = \frac{e_\mathrm{w}}{p}\frac{\partial f}{\partial p} - \frac{1}{p^2} \cdot f \cdot e_\mathrm{w} = \frac{f \cdot e_\mathrm{w}}{p}\left(\frac{1}{f}\frac{\partial f}{\partial p} - \frac{1}{p}\right) = x_\mathrm{w}\left(\frac{1}{f}\frac{\partial f}{\partial p} - \frac{1}{p}\right) \qquad \text{(A.5)}$$

$$\frac{\partial x_\mathrm{w}}{\partial \omega} = \frac{\partial x_\mathrm{w}}{\partial f} \cdot \frac{\partial f}{\partial \omega} = \frac{e_\mathrm{w}}{p} f \qquad \text{(A.6)}$$

$$\frac{\partial x_\mathrm{w}}{\partial \lambda} = \frac{\partial x_\mathrm{w}}{\partial e_\mathrm{w}} \cdot \frac{\partial e_\mathrm{w}}{\partial \lambda} = \frac{f}{p} e_\mathrm{w} \qquad \text{(A.7)}$$

Appendix B

Estimation of the measurement uncertainty

As mentioned in Section 5, the detailed uncertainty contributions considered for the estimation of the measurement uncertainty of T_{fp}, p and x_w in the whole working range of interest are reported in the following tables.

Table B.1: INRIM 03 uncertainty budget for the frost-point temperature, T_{fp}, pressure, p, and water vapour amount fraction, x_w at the following nominal values: T_{fp} = -75 °C, p = 1100 hPa and x_w=1118 nmol·mol^{-1}.

T_{fp} = -75 °C p = 1100 hPa x_w = 1118 nmol·mol^{-1}

Uncertainty budget for T_{fp} / °C

Source of uncertainty	Standard uncertainty	PDF	Sensitivity coefficient	Contribution to combined uncertainty/°C
Saturation temperature repeatability	0.00088 °C	Normal	1	$8.8\cdot10^{-4}$
Saturator temperature uniformity	0.000086 °C	Rectangular	1	$8.6\cdot10^{-4}$
SPRT calibration	0.00025 °C	Normal	1	$2.5\cdot10^{-4}$
Temperature resistance bridge accuracy	0.00043 °C	Rectangular	1	$4.3\cdot10^{-4}$
SPRT drift	0.0017 °C	Rectangular	1	$1.7\cdot10^{-3}$
Self-heating SPRT	0.00066 °C	Asym. Triangular	1	$1.6\cdot10^{-4}$
Adsorption/Desorption	0.034 °C	Normal	1	$3.4\cdot10^{-2}$
Saturation efficiency	0.0068 °C	Rectangular	1	$6.8\cdot10^{-3}$
Combined standard uncertainty, $u_c(T_{fp})$ / °C				**0.034**

Uncertainty budget for p /Pa

Source of uncertainty	Standard uncertainty	PDF	Sensitivity coefficient	Contribution to combined uncertainty/Pa
Pressure control stability	5.4 Pa	U-distribution	1	5.4
Transducer calibration	3.3 Pa	Normal	1	3.3
Long term stability	15.1 Pa	Rectangular	1	15.1
Linearity and temperature effects	7.6 Pa	Rectangular	1	7.6
Resolution	0.03 Pa	Rectangular	1	0.03
Combined standard uncertainty, $u_c(p)$ / Pa				**18.0**

Uncertainty budget for x_w /mol·mol^{-1}

Source of uncertainty	Standard uncertainty	PDF	Sensitivity coefficient	Contribution to combined uncertainty/ mol·mol^{-1}
Saturation pure water vapour pressure, $e(T_{fp})$	0.0002 Pa	Normal	$9.18\cdot10^{-6}$ Pa^{-1}	$2.15\cdot10^{-9}$
Enhancement factor, $f(T_{fp},p)$	0.0005	Normal	$1.13\cdot10^{-6}$	$5.65\cdot10^{-10}$
Frost point temperature, T_{fp}	0.034 °C	Normal	$1.80\cdot10^{-7}$ °C^{-1}	$6.19\cdot10^{-9}$

Pressure, p	18.0 Pa	Normal	$1.71 \cdot 10^{-12}$ Pa^{-1}	$3.09 \cdot 10^{-11}$
Combined standard uncertainty, $u_c(x_w)$ / mol·mol^{-1}				**$6.58 \cdot 10^{-9}$**
Percent relative standard uncertainty, $100 \cdot u_c(x_w) / x_w$				**0.59**

Table B.2: INRIM 03 uncertainty budget for the frost-point temperature, T_{fp}, pressure, p, and water vapour amount fraction, x_w at the following nominal values: T_{fp} = -75 °C, p = 200 hPa and x_w= 6104 nmol·mol^{-1}.

T_{fp} = -75 °C p = 200 hPa x_w = 6104 nmol·mol^{-1}

Uncertainty budget for T_{fp} / °C

Source of uncertainty	Standard uncertainty	PDF	Sensitivity coefficient	Contribution to combined uncertainty / °C
Saturation temperature repeatability	0.00077 °C	Normal	1	$7.7 \cdot 10^{-4}$
Saturator temperature uniformity	0.00028 °C	Rectangular	1	$2.8 \cdot 10^{-4}$
SPRT calibration	0.00025 °C	Normal	1	$2.5 \cdot 10^{-4}$
Temperature resistance bridge accuracy	0.00043 °C	Rectangular	1	$4.3 \cdot 10^{-4}$
SPRT drift	0.0017 °C	Rectangular	1	$1.7 \cdot 10^{-3}$
Self-heating SPRT	0.00066 °C	Asym. Triangular	1	$1.6 \cdot 10^{-4}$
Adsorption/Desorption	0.032 °C	Normal	1	$3.2 \cdot 10^{-2}$
Saturation efficiency	0.00082 °C	Rectangular	1	$8.2 \cdot 10^{-4}$
Combined standard uncertainty, $u_c(T_{fp})$ / °C				**0.032**

Uncertainty budget for p /Pa

Source of uncertainty	Standard uncertainty	PDF	Sensitivity coefficient	Contribution to combined uncertainty / Pa
Pressure control stability	3.7 Pa	U-distribution	1	3.7
Transducer calibration	2.0 Pa	Normal	1	2.0
Long term stability	15.1 Pa	Rectangular	1	15.1
Linearity and temperature effects	7.6 Pa	Rectangular	1	7.6
Resolution	0.03 Pa	Rectangular	1	0.03
Combined standard uncertainty, $u_c(p)$ /Pa				**17.4**

Uncertainty budget for x_w /mol·mol^{-1}

Source of uncertainty	Standard uncertainty	PDF	Sensitivity coefficient	Contribution to combined uncertainty/ mol·mol^{-1}
Saturation pure water vapour pressure, $e(T_{fp})$	0.00024 Pa	Normal	$5.01 \cdot 10^{-5}$ Pa^{-1}	$1.18 \cdot 10^{-8}$
Enhancement factor, $f(T_{fp},p)$	0.000087	Normal	$6.21 \cdot 10^{-6}$	$5.39 \cdot 10^{-10}$
Frost point temperature, T_{fp}	0.032 °C	Normal	$9.74 \cdot 10^{-7}$ °C^{-1}	$3.12 \cdot 10^{-8}$
Pressure, p	17.4 Pa	Normal	$2.64 \cdot 10^{-10}$ Pa^{-1}	$4.59 \cdot 10^{-9}$
Combined standard uncertainty, $u_c(x_w)$ / mol·mol^{-1}				**$3.37 \cdot 10^{-8}$**

Percent relative standard uncertainty, 100·$u_c(x_w)$ / x_w	**0.55**

Table B.3: INRIM 03 uncertainty budget on the frost-point temperature, T_{fp}, pressure, p, and water vapour amount fraction, x_w at the following nominal values T_{fp} = -90 °C, p = 1100 hPa and x_w= 89 nmol·mol^{-1}.

T_{fp} = -90 °C p = 1100 hPa x_w = 89 nmol·mol^{-1}				
Uncertainty budget for T_{fp} / °C				
Source of uncertainty	Standard uncertainty	PDF	Sensitivity coefficient	Contribution to combined uncertainty / °C
Saturation temperature repeatability	0.00079 °C	Normal	1	$7.9\cdot10^{-4}$
Saturator temperature uniformity	0.00059 °C	Rectangular	1	$5.9\cdot10^{-4}$
SPRT calibration	0.00025 °C	Normal	1	$2.5\cdot10^{-4}$
Temperature resistance bridge accuracy	0.00043 °C	Rectangular	1	$4.3\cdot10^{-4}$
SPRT drift	0.0017 °C	Rectangular	1	$1.7\cdot10^{-3}$
Self-heating SPRT	0.00066 °C	Asym. Triangular	1	$1.6\cdot10^{-4}$
Adsorption/Desorption	0.027 °C	Normal	1	$2.7\cdot10^{-2}$
Saturation efficiency	0.012 °C	Rectangular	1	$1.2\cdot10^{-2}$
Combined standard uncertainty, $u_c(T_{fp})$ / °C				**0.030**
Uncertainty budget for p /Pa				
Source of uncertainty	Standard uncertainty	PDF	Sensitivity coefficient	Contribution to combined uncertainty/ Pa
Pressure control stability	6.8 Pa	U-distribution	1	6.8
Transducer calibration	3.1 Pa	Normal	1	3.1
Long term stability	15.1 Pa	Rectangular	1	15.1
Linearity and temperature effects	7.6 Pa	Rectangular	1	7.6
Resolution	0.03 Pa	Rectangular	1	0.03
Combined standard uncertainty, $u_c(p)$ / Pa				**18.5**
Uncertainty budget for x_w /mol·mol^{-1}				
Source of uncertainty	Standard uncertainty	PDF	Sensitivity coefficient	Contribution to combined uncertainty/ mol·mol^{-1}
Saturation pure water vapour pressure, $e(T_{fp})$	0.000023 Pa	Normal	$9.18\cdot10^{-6}$ Pa^{-1}	$2.09\cdot10^{-10}$
Enhancement factor, $f(T_{fp},p)$	0.00063	Normal	$8.39\cdot10^{-8}$	$5.24\cdot10^{-11}$
Frost point temperature, T_{fp}	0.030 °C	Normal	$1.57\cdot10^{-8}$ °C^{-1}	$4.69\cdot10^{-10}$
Pressure, p	18.5 Pa	Normal	$1.41\cdot10^{-14}$ Pa^{-1}	$2.61\cdot10^{-13}$
Combined standard uncertainty, $u_c(x_w)$ / mol·mol^{-1}				**$5.17\cdot10^{-10}$**
Percent relative standard uncertainty, 100·$u_c(x_w)$ / x_w				**0.58**

Table B.4: INRIM 03 uncertainty budget on the frost-point temperature, T_{fp}, pressure, p, and water vapour amount fraction, x_w at the following nominal values T_{fp} = -90 °C, p = 200 hPa and x_w= 484 nmol·mol^{-1}.

T_{fp} = -90 °C p = 200 hPa x_w = 484 nmol·mol^{-1}				
Uncertainty budget for T_{fp} / °C				
Source of uncertainty	Standard uncertainty	PDF	Sensitivity coefficient	Contribution to combined uncertainty/ °C
Saturation temperature repeatability	0.0017 °C	Normal	1	$1.7 \cdot 10^{-3}$
Saturator temperature uniformity	0.00014 °C	Rectangular	1	$1.4 \cdot 10^{-4}$
SPRT calibration	0.00025 °C	Normal	1	$2.5 \cdot 10^{-4}$
Temperature resistance bridge accuracy	0.00043 °C	Rectangular	1	$4.3 \cdot 10^{-4}$
SPRT drift	0.0017 °C	Rectangular	1	$1.7 \cdot 10^{-3}$
Self-heating SPRT	0.00066 °C	Asym. Triangular	1	$1.6 \cdot 10^{-4}$
Adsorption/Desorption	0.027 °C	Normal	1	$2.7 \cdot 10^{-2}$
Saturation efficiency	0.0016 °C	Rectangular	1	$1.6 \cdot 10^{-3}$
Combined standard uncertainty, $u_c(T_{fp})$ / °C				**0.027**
Uncertainty budget for p /Pa				
Source of uncertainty	Standard uncertainty	PDF	Sensitivity coefficient	Contribution to combined uncertainty/ Pa
Pressure control stability	4.1 Pa	U-distribution	1	4.1
Transducer calibration	2.0 Pa	Normal	1	2.0
Long term stability	15.1 Pa	Rectangular	1	15.1
Linearity and temperature effects	7.6 Pa	Rectangular	1	7.6
Resolution	0.03 Pa	Rectangular	1	0.03
Combined standard uncertainty, $u_c(p)$ / Pa				**17.5**
Uncertainty budget for x_w /mol·mol^{-1}				
Source of uncertainty	Standard uncertainty	Probability distribution	Sensitivity Coefficient	Contribution to combined uncertainty/ mol·mol^{-1}
Saturation pure water vapour pressure, $e(T_{fp})$	0.000023 Pa	Normal	$5.01 \cdot 10^{-5}$ Pa^{-1}	$1.14 \cdot 10^{-9}$
Enhancement factor, $f(T_{fp},p)$	0.00011	Normal	$4.62 \cdot 10^{-7}$	$5.17 \cdot 10^{-11}$
Frost point temperature, T_{fp}	0.027 °C	Normal	$8.49 \cdot 10^{-8}$ °C^{-1}	$2.32 \cdot 10^{-9}$
Pressure, p	17.5 Pa	Normal	$1.90 \cdot 10^{-11}$ Pa^{-1}	$3.32 \cdot 10^{-10}$
Combined standard uncertainty, $u_c(x_w)$ / mol·mol^{-1}				**$2.61 \cdot 10^{-9}$**
Percent relative standard uncertainty, $100 \cdot u_c(x_w)$ / x_w				**0.54**

Table B.5: INRIM 03 uncertainty budget on the frost-point temperature, T_{fp}, pressure, p, and water vapour amount fraction, x_w at the following nominal values T_{fp} = -95 °C, p = 1100 hPa and x_w= 35 nmol·mol^{-1}.

T_{fp} = -95 °C p = 1100 hPa x_w = 35 nmol·mol^{-1}				
Uncertainty budget for T_{fp} / °C				
Source of uncertainty	Standard uncertainty	PDF	Sensitivity coefficient	Contribution to combined uncertainty / °C
Saturation temperature repeatability	0.0013 °C	Normal	1	$1.3 \cdot 10^{-3}$
Saturator temperature uniformity	0.0016 °C	Rectangular	1	$1.6 \cdot 10^{-3}$
SPRT calibration	0.00025 °C	Normal	1	$2.5 \cdot 10^{-4}$
Temperature resistance bridge accuracy	0.00043 °C	Rectangular	1	$4.3 \cdot 10^{-4}$
SPRT drift	0.0017 °C	Rectangular	1	$1.7 \cdot 10^{-3}$
Self-heating SPRT	0.00066 °C	Asym. Triangular	1	$1.6 \cdot 10^{-4}$
Adsorption/Desorption	0.026 °C	Normal	1	$2.6 \cdot 10^{-2}$
Saturation efficiency	0.012 °C	Rectangular	1	$1.2 \cdot 10^{-2}$
Combined standard uncertainty, $u_c(T_{fp})$ / °C				**0.029**
Uncertainty budget for p /Pa				
Source of uncertainty	Standard uncertainty	PDF	Sensitivity coefficient	Contribution to combined uncertainty/ Pa
Pressure control stability	5.9 Pa	U-distribution	1	5.9
Transducer calibration	3.1 Pa	Normal	1	3.1
Long term stability	15.1 Pa	Rectangular	1	15.1
Linearity and temperature effects	7.6 Pa	Rectangular	1	7.6
Resolution	0.03 Pa	Rectangular	1	0.03
Combined standard uncertainty, $u_c(p)$ / Pa				**18.2**
Uncertainty budget for x_w /mol·mol^{-1}				
Source of uncertainty	Standard uncertainty	PDF	Sensitivity coefficient	Contribution to Standard uncertainty/ mol·mol^{-1}
Saturation pure water vapour pressure, $e(T_{fp})$	0.0000098 Pa	Normal	$9.18 \cdot 10^{-6}$ Pa^{-1}	$8.96 \cdot 10^{-11}$
Enhancement factor, $f(T_{fp},p)$	0.00067	Normal	$3.31 \cdot 10^{-8}$	$2.22 \cdot 10^{-11}$
Frost point temperature, T_{fp}	0.029 °C	Normal	$6.56 \cdot 10^{-9}$ °C^{-1}	$1.88 \cdot 10^{-10}$
Pressure, p	18.2 Pa	Normal	$1.10 \cdot 10^{-14}$ Pa^{-1}	$1.99 \cdot 10^{-13}$
Combined standard uncertainty, $u_c(x_w)$ / mol·mol^{-1}				**$2.10 \cdot 10^{-10}$**
Percent relative standard uncertainty, $100 \cdot u_c(x_w)$ / x_w				**0.60**

Table B.6: INRIM 03 uncertainty budget on the frost-point temperature, T_{fp}, pressure, p, and water vapour amount fraction, x_w at the following nominal values T_{fp} = -95 °C, p = 200 hPa and x_w= 189 nmol·mol^{-1}.

T_{fp} = -95 °C p = 200 hPa x_w = 189 nmol·mol^{-1}

Uncertainty budget for T_{fp} / °C

Source of uncertainty	Standard uncertainty	PDF	Sensitivity coefficient	Contribution to combined uncertainty/ °C
Saturation temperature repeatability	0.00068 °C	Normal	1	$6.8\cdot10^{-4}$
Saturator temperature uniformity	0.00013 °C	Rectangular	1	$1.3\cdot10^{-4}$
SPRT calibration	0.00025 °C	Normal	1	$2.5\cdot10^{-4}$
Temperature resistance bridge accuracy	0.00043 °C	Rectangular	1	$4.3\cdot10^{-4}$
SPRT drift	0.0017 °C	Rectangular	1	$1.7\cdot10^{-3}$
Self-heating SPRT	0.00066 °C	Asym. Triangular	1	$1.6\cdot10^{-4}$
Adsorption/Desorption	0.026 °C	Normal	1	$2.6\cdot10^{-2}$
Saturation efficiency	0.0038	Rectangular	1	$3.8\cdot10^{-3}$
Combined standard uncertainty, $u_c(T_{fp})$ / °C				**0.026**

Uncertainty budget for p /Pa

Source of uncertainty	Standard uncertainty	PDF	Sensitivity coefficient	Contribution to combined uncertainty/ Pa
Pressure control stability	4.1 Pa	U-distribution	1	4.1
Transducer calibration	2.0 Pa	Normal	1	2.0
Long term stability	15.1 Pa	Rectangular	1	15.1
Linearity and temperature effects	7.6 Pa	Rectangular	1	7.6
Resolution	0.03 Pa	Rectangular	1	0.03
Combined standard uncertainty, $u_c(p)$ / Pa				**17.5**

Uncertainty budget for x_w /mol·mol^{-1}

Source of uncertainty	Standard uncertainty	PDF	Sensitivity coefficient	Contribution to combined uncertainty/ mol·mol^{-1}
Saturation pure water vapour pressure, $e(T_{fp})$	0.0000098 Pa	Normal	$5.01\cdot10^{-5}$ Pa^{-1}	$4.87\cdot10^{-10}$
Enhancement factor, $f(T_{fp},P)$	0.00012	Normal	$1.82\cdot10^{-7}$	$2.21\cdot10^{-11}$
Frost point temperature, T_{fp}	0.026 °C	Normal	$3.53\cdot10^{-8}$ °C^{-1}	$9.23\cdot10^{-10}$
Pressure, p	17.5 Pa	Normal	$7.38\cdot10^{-12}$ Pa^{-1}	$1.29\cdot10^{-10}$
Combined standard uncertainty, $u_c(x_w)$ / mol·mol^{-1}				**$1.05\cdot10^{-9}$**
Percent relative standard uncertainty, $100\cdot u_c(x_w)$ / x_w				**0.56**

Table B.7: INRIM 03 uncertainty budget on the frost-point temperature, T_{fp}, pressure, p, and water vapour amount fraction, x_w at the following nominal values: T_{fp} = -100 °C, p = 1100 hPa and x_w= 13 nmol·mol^{-1}.

T_{fp} = -100 °C p = 1100 hPa x_w = 13 nmol·mol^{-1}

Uncertainty budget for T_{fp} / °C

Source of uncertainty	Standard uncertainty	PDF	Sensitivity coefficient	Contribution to combined uncertainty / °C
Saturation temperature repeatability	0.0017 °C	Normal	1	$1.7\cdot10^{-3}$
Saturator temperature uniformity	0.00049 °C	Rectangular	1	$4.9\cdot10^{-4}$
SPRT calibration	0.00025 °C	Normal	1	$2.5\cdot10^{-4}$
Temperature resistance bridge accuracy	0.00043 °C	Rectangular	1	$4.3\cdot10^{-4}$
SPRT drift	0.0017 °C	Rectangular	1	$1.7\cdot10^{-3}$
Self-heating SPRT	0.00066 °C	Asym. Triangular	1	$1.6\cdot10^{-4}$
Adsorption/Desorption	0.025 °C	Normal	1	$2.5\cdot10^{-2}$
Saturation efficiency	0.13 °C	Rectangular	1	$1.3\cdot10^{-1}$
Combined standard uncertainty, $u_c(T_{fp})$ / °C				**0.131**

Uncertainty budget for p /Pa

Source of uncertainty	Standard uncertainty	PDF	Sensitivity coefficient	Contribution to combined uncertainty/ Pa
Pressure control stability	6.0 Pa	U-distribution	1	6.0
Transducer calibration	3.1 Pa	Normal	1	3.1
Long term stability	15.1 Pa	Rectangular	1	15.1
Linearity and temperature effects	7.6 Pa	Rectangular	1	7.6
Resolution	0.03 Pa	Rectangular	1	0.03
Combined standard uncertainty, $u_c(p)$ / Pa				**18.2**

Uncertainty budget for x_w /mol·mol^{-1}

Source of uncertainty	Standard uncertainty	PDF	Sensitivity coefficient	Contribution to Standard uncertainty/ mol·mol^{-1}
Saturation pure water vapour pressure, $e(T_{fp})$	0.0000048 Pa	Normal	$9.19\cdot10^{-6}$ Pa^{-1}	$4.45\cdot10^{-11}$
Enhancement factor, $f(T_{fp},p)$	0.00071	Normal	$1.55\cdot10^{-8}$	$1.10\cdot10^{-11}$
Frost point temperature, T_{fp}	0.131 °C	Normal	$3.20\cdot10^{-9}$ °C^{-1}	$4.18\cdot10^{-10}$
Pressure, p	18.2 Pa	Normal	$1.14\cdot10^{-14}$ Pa^{-1}	$2.08\cdot10^{-13}$
Combined standard uncertainty, $u_c(x_w)$ / mol·mol^{-1}				**$4.21\cdot10^{-10}$**
Percent relative standard uncertainty, 100·$u_c(x_w)$ / x_w				**3.24**

Table B.8: INRIM 03 uncertainty budget on the frost-point temperature, T_{fp}, pressure, p, and water vapour amount fraction, x_w at the following nominal values: T_{fp} = -100 °C, p = 200 hPa and x_w= 70 nmol·mol^{-1}.

T_{fp} = -100 °C p = 200 hPa x_w = 70 nmol·mol^{-1}

Uncertainty budget for T_{fp} / °C

Source of uncertainty	Standard uncertainty	PDF	Sensitivity coefficient	Contribution to combined uncertainty/ °C
Saturation temperature repeatability	0.0014 °C	Normal	1	$1.4\cdot10^{-3}$
Saturator temperature uniformity	0.00024 °C	Rectangular	1	$2.4\cdot10^{-4}$
SPRT calibration	0.00025 °C	Normal	1	$2.5\cdot10^{-4}$
Temperature resistance bridge accuracy	0.00043 °C	Rectangular	1	$4.3\cdot10^{-4}$
SPRT drift	0.0017 °C	Rectangular	1	$1.7\cdot10^{-3}$
Self-heating SPRT	0.00066 °C	Asym. Triangular	1	$1.6\cdot10^{-4}$
Adsorption/Desorption	0.025 °C	Normal	1	$2.5\cdot10^{-2}$
Saturation efficiency	0.0061	Rectangular	1	$6.1\cdot10^{-3}$
Combined standard uncertainty, $u_c(T_{fp})$ / °C				**0.026**

Uncertainty budget for p /Pa

Source of uncertainty	Standard uncertainty	PDF	Sensitivity coefficient	Contribution to combined uncertainty/ Pa
Pressure control stability	3.2 Pa	U-distribution	1	3.2
Transducer calibration	2.0 Pa	Normal	1	2.0
Long term stability	15.1 Pa	Rectangular	1	15.1
Linearity and temperature effects	7.6 Pa	Rectangular	1	7.6
Resolution	0.03 Pa	Rectangular	1	0.03
Combined standard uncertainty, $u_c(p)$ / Pa				**17.3**

Uncertainty budget for x_w /mol·mol^{-1}

Source of uncertainty	Standard uncertainty	PDF	Sensitivity coefficient	Contribution to combined uncertainty/ mol·mol^{-1}
Saturation pure water vapour pressure, $e(T_{fp})$	0.0000048 Pa	Normal	$5.00\cdot10^{-5}$ Pa^{-1}	$2.43\cdot10^{-10}$
Enhancement factor, $f(T_{fp},P)$	0.00013	Normal	$8.51\cdot10^{-8}$	$1.10\cdot10^{-11}$
Frost point temperature, T_{fp}	0.026 °C	Normal	$1.72\cdot10^{-8}$ °C^{-1}	$4.41\cdot10^{-10}$
Pressure, p	17.3 Pa	Normal	$3.42\cdot10^{-12}$ Pa^{-1}	$5.92\cdot10^{-11}$
Combined standard uncertainty, $u_c(x_w)$ / mol·mol^{-1}				**$5.07\cdot10^{-10}$**
Percent relative standard uncertainty, $100\cdot u_c(x_w)$ / x_w				**0.72**

References

[1] European Commission, Secretariat-General. Document 52019DC0640 “COMMUNICATION FROM THE COMMISSION TO THE EUROPEAN PARLIAMENT, THE EUROPEAN COUNCIL, THE COUNCIL, THE EUROPEAN ECONOMIC AND SOCIAL COMMITTEE AND THE COMMITTEE OF

THE REGIONS The European Green Deal", COM/2019/640 final. Available online: https://eur-lex.europa.eu/legal-content/EN/TXT/?uri=COM:2019:640:FIN

[2] Cuccaro et al., "Development of a low frost-point generator operating at sub-atmospheric pressure", Meas. Sci. Technol. 29 (2018) 054002 (12pp).

[3] Abe H and Kitano H, 2006 Development humidity standard in trace-moisture region: characteristics of humidity generation of diffusion tube humidity generator, Sensors Actuators A 128 202–208.

[4] Abe H and Kitano H, 2007, Improvement of flow and pressure controls in diffusion-tube humidity generator: performance evaluation of trace-moisture generation using cavity ring-down spectroscopy, Sensors Actuators A 136 723–9.

[5] Abe H, Tanaka H and Kitano H, 2008, Uncertainty analysis of evapouration rate in magnetic suspension balance/ diffusion-tube humidity generator, Int. J. Thermophys. 29 1555–66.

[6] Amano M. and Abe H, 2023, Primary measurement standards for trace moisture in multiple gases: extension of gas species to He and O2, Metrologia 60 045003.

[7] Sang-Wook Lee *et al,* 2021, "Development of a new KRISS low frost-point generator with improved uncertainty from 7 nmol·mol^{-1} to 1000 nmol·mol^{-1}", Metrologia 58 065002.

[8] Choi B I, Nham H S, Woo S B, Kim J C and Kwon S Y 2008. The new KRISS low frost-point humidity generator Int. J. Thermophys. 29 1578–88

[9] Choi B I, Kim J C and Woo S B 2012 Uncertainty of the Kriss low frost-point humidity generator Int. J. Thermophys. 33 1559–67.

[10] Choi B I, Lee S-W, Kim J C and Woo S B 2015 Extension of humidity standards to−105 ◦C frost point Int. J. Thermophys. 36 2231–41.

[11] S. Wettstein, D. Mutter, Design and validation of the MBW standard humidity generators, Int. J. Thermophys. (2018) 39:116.

[12] M. Stevens and R. Benyon, Conceptual design of a low-range humidity standard generator, Proc. of the Third International Symposium on Humidity and Moisture, National Physical Laboratory, Teddington (UK) 1998, Vol. 1, p. 103.

[13] Sonntag D 1990 Important new values of the physical constants of 1986, vapour pressure formulations based on the ITS-90, and psychrometer formulae Z. Meteorol. 40 340-4.

[14] IAPWS, Revised Release on the Pressure along the Melting and Sublimation Curves of Ordinary Water Substance (2011). Available from http://www.iapws.org

[15] W. Wagner, T. Riethmann, R. Feistel, A.H. Harvey, New equations for the sublimation pressure and melting pressure of H_2O Ice Ih. J. Phys. Chem. Ref. Data 40, 043103 (2011).

[16] W. Bögel 1977 Neue Näherungsgleichungen für den sättigungsdruck des Wasserdampfes und für die in der Meteorologie gebräuchlichen Luftfeuchte-Parameter. DFVLR-Institut für Physik der Atmosphäre Oberpfaffenhofen 1977, DLR-FB 77-52, 158 p.

[17] J Lovell-Smith, An expression for the uncertainty in the water vapour pressure enhancement factor for moist air, Metrologia 44 (2007) L49-L52.

[18] J Lovell-Smith, The propagation of uncertainty for humidity calculations, Metrologia 46 (2009) 607-615.